MOX–Report No. 50/2012

A second order accurate numerical model for multiphase underexpanded volcanic jets

Carcano, S.; Bonaventura, L.; Neri, A.; Esposti Ongaro, T.

A second order accurate numerical model for multiphase underexpanded volcanic jets

Susanna Carcano [1], Luca Bonaventura[1]
Augusto Neri [2], Tomaso Esposti Ongaro [2]

November 13, 2012

[1] MOX – Modelling and Scientific Computing,
Dipartimento di Matematica "F. Brioschi", Politecnico di Milano
Via Bonardi 9, 20133 Milano, Italy
susanna.carcano@mail.polimi.it, luca.bonaventura@polimi.it

[2] Istituto Nazionale di Geofisica e Vulcanologia
Sezione di Pisa
Via della Faggiola, 32, 56126, Pisa, Italy
neri@pi.ingv.it, ongaro@pi.ignv.it

Keywords: Volcanic eruptions, supersonic jets, multiphase flows, implicit methods, finite volume methods.

AMS Subject Classification: 35L65, 35Q86, 65M08, 65Y05, 76T15.

Abstract

An improved version of the PDAC (Pyroclastic Dispersal Analysis Code) numerical model for the simulation of multiphase volcanic flows is presented and validated for the simulation of multiphase volcanic jets in supersonic regimes. The present version of PDAC includes second-order time and space discretizations and fully multidimensional advection discretizations, in order to reduce numerical diffusion and enhance the accuracy of the original model. The resulting numerical model is tested against the problem of jet decompression in both two and three dimensions. For homogeneous jets, numerical results show a good quantitative agreement with experimental results on the laboratory scale in terms of Mach disk location (Lewis and Carlson, 1964). For multiphase jets, we consider monodisperse and polydisperse mixtures of particles with different diameter. For fine particles, for which the pseudogas limit is valid, the multiphase model correctly reproduces predictions of the pseudogas model. We obtain that particles are in mechanical and thermal equilibrium with the gas phase and the jet decompression structure is in quantitative agreement with pseudogas results (Ogden et al., 2008b). For both fine and coarse particles, we measure the importance of multiphase effects with relation to the characteristic time scales of multiphase jets and we quantify how particles affect the average jet dynamics in terms of pressure, mixture density, vertical velocity and temperature. Furthermore, time dependent vent conditions are introduced, in order to achieve numerical simulation of eruption regimes characterized by transient jet behaviour. We show how in case of rapid change in vent conditions, volcanic jet structures do not evolve through a succession of steady state configurations and the transition between different flow conditions can result in the collapse of the volcanic column.

Introduction

During explosive volcanic eruptions a mixture of gases, magma fragments, crystals and eroded rocks is injected in the atmosphere at high velocity, pressure and temperature. The diverse and unpredictable behaviour of injection conditions (and the consequent variability of eruptive styles) depends on the complex rheology of magma and on the nonlinear processes leading to the fragmentation of the viscous melt into a polydisperse mixture of gases and particles (Gonnermann and Manga, 2007). Nonetheless, the explosive character of an eruption is always associated to the rapid decompression and the consequent abrupt expansion of gases in the magma (the exsolved magmatic volatiles in magmatic eruptions, vaporized free water or hydrothermal fluids in hydromagmatic and phreatomagmatic eruptions) (Parfitt and Wilson, 2008). Under such conditions, in the proximity of the volcanic vent, the erupted multiphase mixture is accelerated abruptly and can manifest the features of supersonic flows (Kieffer, 1984; Woods and Bower, 1995; Ogden et al., 2008b; Orescanin et al., 2010).

After decompression, on the other hand, the eruption dynamics is mainly influenced by subsonic turbulent mixing and mass and thermal exchange between the eruptive mixture and the atmosphere. Column behaviour is indeed controlled by the balance between its negative buoyancy, associated to the load of solid particles, and the positive buoyancy due to air heating and expansion. Depending upon the efficiency of the turbulent entrainment the gas-particle mixture can form a buoyant plume in the atmosphere or collapse under its particle load forming pyroclastic density currents (Valentine, 1998).

A general understanding of the transport dynamics of pyroclasts in the atmosphere has been first achieved by describing the eruptive mixture as homogeneous, i.e., by assuming kinetic and thermal equilibrium between gas and particles and by solving the resulting transport equations under simplified conditions (e.g., assuming cylindrical symmetry, point source, steady state conditions) (Wilson, 1976; Woods, 1988; Sparks et al., 1997). Homogeneous models based on the kinetic and thermal equilibrium assumptions have also been extended to two and three dimensions (Oberhuber et al., 1998; Suzuki et al., 2005; Ogden et al., 2008a), to carry out numerical simulations of volcanic processes at the large scale, highlighting the key roles of environmental atmospheric conditions (Graf et al., 1999), large-eddy turbulence (Suzuki and Koyaguchi, 2010), vent overpressure (Ogden et al., 2008b) and boundary-layer processes (Doronzo

et al., 2012). However, the detailed reconstruction of well documented eruptions and the growing need to quantify and map the hazards associated to future explosive events require the simulation of full eruptive scenarios. To this aim, eruption models able to incorporate the main dynamic processes and more realistic input conditions are needed. The problem, in its general multidimensional and unsteady formulation, is thus extremely challenging due to the multiphase nature of the flow and to its multiscale features.

Mathematical models based on multiphase flow formulation have been proposed starting from the late 1980's (Valentine and Wohletz, 1989; Dobran et al., 1993) but have become more popular in the last decade (Dartevelle et al., 2004; Pelanti and LeVeque, 2006; Dufek and Bergantz, 2007; Esposti Ongaro et al., 2007) also thanks to the impressive development of computational techniques allowing the solution of the complicated set of transport equations on modern high-performance parallel computers.

This work is based on the application and enhancement of the PDAC model, (Pyroclastic Dispersal Analysis Code), described in Section 1 and in more detail in Neri et al. (2003) and Esposti Ongaro et al. (2007), to solve the multiphase flow equations for a mixture of volcanic gases and pyroclasts in non-equilibrium conditions, when they can exchange momentum and heat. The PDAC numerical solution procedure is based on the original algorithm by Harlow and Amsden (1975), in which a first order semi-implicit treatment for multiphase flows was combined with simple, donor cell based finite volume conservative advection schemes. Typically, such first-order techniques introduce large amounts of numerical diffusion. Esposti Ongaro et al. (2007) extended the first-order spatial discretization to second order in each separate spatial direction, by adopting the one-dimensional MUSCL scheme (Sweby, 1984), as also common in other multiphase flow codes (e.g., MFIX in Syamlal et al., 1993, Syamlal, 1998), but did not modify the semi-implicit time-advancement scheme based on the backward Euler discretization of time derivatives. The resulting numerical method was effective, but its results still display significant amounts numerical diffusion, especially in multi-dimensional simulations, which implies the need for very high spatial resolution and small time-steps to achieve an accurate simulation.

The objective of this work is to modify the numerical algorithm in order to make it more suitable to the resolution of the near-vent decompression dynamics, potentially involving supersonic regimes and shock waves, and the three-dimensional, transient dynamics of turbulent eddies, controlling, for example, the atmospheric air

4

entrainment. We propose an improvement of the original PDAC numerical model to achieve higher accuracy and robustness in the resolution of compressible regimes, while reducing the numerical diffusion that may significantly damp turbulent eddies in subsonic regimes. The resulting model is applied to the simulation of the decompression structures that form above the vent in the very first part of explosive events.

Although in the context of volcanic eruption simulations a rigorous model verification or validation are perhaps impossible (Oreskes et al., 1994), three-dimensional multiphase flow models have demonstrated, in the last years, the potential for providing a good representation of the actual processes occurring in the real system (Dufek and Bergantz, 2007; Esposti Ongaro et al., 2012). The validation of numerical results against empirical observations of well-documented eruptions, together with the congruence of numerical benchmarks with experimental and theoretical results, are at present the only available instruments to assess the "empirical adequacy" (Oreskes et al., 1994) of models to simulate eruptive scenarios. As it will be demonstrated below, the results of the present model are in good qualitative and quantitative agreement with a number of experimental and numerical results available in the literature.

In Section 1, we describe briefly the PDAC model and the simplifing assumption adopted in the present work. In Sections 2 and 3, the present, improved version of the PDAC numerical method is described. More specifically, a second order Crank-Nicolson type time discretization (Crank and Nicolson, 1947) and a more accurate and fully multidimensional advection scheme (LeVeque, 1996) are introduced in the framework of the semi-implicit approach proposed by Harlow and Amsden (1975). Numerical benchmarks and comparison with analogous results obtained with other models are presented in Sections 4 and 5. Finally, some conclusions and perspectives for future work are presented in Section 6, where proposals for more substantial model reformulations and improvements are discussed.

1 Multiphase flow equations

In this work we employ the same model equations as in the original PDAC model proposed by Neri et al. (2003). They are appropriate to describe the injection and dispersal of a hot and high velocity gas-pyroclast mixture in a standard reference atmosphere. The model is based on the following main hypotheses:

- the solid particles and the gas are considered as interpenetrating continua, following an Eulerian-Eulerian approach;

- the gas phase is compressible and obeys the ideal gas law;

- mass transfer processes due to phase changes and chemical reactions are neglected;

- solid particles are assumed to be spherical and each class is assumed to consist of particles of equal radius and density;

- particles are assumed to maintain their original size, thus neglecting the effect of any secondary fragmentation or aggregation process on the large-scale dispersal dynamics;

- the heat transfer between different solid phases, as well as the viscous dissipation effects, are neglected due to their second-order effect in comparison with advection, conduction and gas-particle heat exchange.

While in general turbulence and other dissipative effects cannot be neglected, for simplicity we will only focus in this work on inviscid equations and regimes. As reported in detail in Appendix A, a scale analysis of the model equations shows that the typical values of the Reynolds number $Re = \frac{\rho U L}{\mu}$ and the Péclet number $Pe = \frac{c_p \rho U L}{k}$ in a volcanic jet vary from 10^6 to 10^{11} in the regimes of interest. Consequently, the only dissipative terms retained in the following are those representing frictional processes between the gas and the solid phase. However, all the physical processes neglected in this presentation are actually accounted for in the complete PDAC model, in the same way as in the original model proposed in Neri et al. (2003), to which we refer for a more complete description of these terms.

The gas phase is composed of different chemical components leaving the crater, such as water vapor and carbon dioxide, and atmospheric air, considered as a single chemical component. The pyroclasts are described by N classes of solid particles, each one characterized by a diameter, density, specific heat and thermal conductivity. In the following sections, we will denote with the subscript $s = 1 \ldots N$ the classes of solid particles and with $l = 1 \ldots M$ the chemical components of the gas phase g. The model variables can be defined as follows:

- ϵ_g, ϵ_s = volumetric fractions of gas and solid particles; if V is the representative volume and V_g and V_s are the volumes occupied by gas and particles, respectively, the gas and solid volume fractions are defined by $\epsilon_g = V_g/V$, $\epsilon_s = V_s/V$;

- ρ_g, ρ_s = microscopic densities of gas and solid particles;
- y_l = mass fractions of the gas components;
- $\mathbf{v}_g$, $\mathbf{v}_s$ = velocities of gas and solid particles;
- p_g = gas pressure;
- h_g, h_s = enthalpies of gas and solid particles;
- T_g, T_s = temperatures of gas and solid particles.

The model consists of $5(N+1)+M$ coupled partial differential equations for the independent variables p_g, ρ_g, ϵ_s, $\mathbf{v}_s$, h_s (or T_s), y_l, with $s = g, 1 \ldots N$ and $l = 1 \ldots M$. The mass conservation equations for the gas phase g, the s-th solid phase and the l-th gas chemical component are

$$\frac{\partial(\epsilon_g \rho_g)}{\partial t} + \nabla \cdot (\epsilon_g \rho_g \mathbf{v}_g) \quad = 0, \tag{1}$$

$$\frac{\partial(\epsilon_s \rho_s)}{\partial t} + \nabla \cdot (\epsilon_s \rho_s \mathbf{v}_s) \quad = 0, \quad s = 1 \ldots N, \tag{2}$$

$$\frac{\partial(\epsilon_l \rho_l y_l)}{\partial t} + \nabla \cdot (\epsilon_l \rho_l y_l \mathbf{v}_g) \quad = 0, \quad l = 1 \ldots M. \tag{3}$$

The momentum balance equations for the gas phase and the s-th solid phase, for all $s = 1 \ldots N$ with $p \neq s$, can be written as

$$\frac{\partial(\epsilon_g \rho_g \mathbf{v}_g)}{\partial t} + \nabla \cdot (\epsilon_g \rho_g \mathbf{v}_g \mathbf{v}_g) =$$

$$= -\epsilon_g \nabla p_g + \epsilon_g \rho_g \mathbf{g} + \sum_{s=1}^{N} D_{s,g}(\mathbf{v}_s - \mathbf{v}_g), \tag{4}$$

$$\frac{\partial(\epsilon_s \rho_s \mathbf{v}_s)}{\partial t} + \nabla \cdot (\epsilon_s \rho_s \mathbf{v}_s \mathbf{v}_s) =$$

$$= -\epsilon_s \nabla p_g + \epsilon_s \rho_s \mathbf{g} + \sum_{p=1}^{N} D_{p,s}(\mathbf{v}_p - \mathbf{v}_s) + D_{g,s}(\mathbf{v}_g - \mathbf{v}_s). \tag{5}$$

Here, $D_{p,s}$ represents the drag coefficient describing the interaction between the phase p and the phase s and $\mathbf{g}$ denotes the gravitational acceleration vector. The energy balance equations for the gas phase and the solid phases $s = 1 \ldots N$ are written in terms of their enthalpies:

$$\frac{\partial(\epsilon_g \rho_g h_g)}{\partial t} + \nabla \cdot (\epsilon_g \rho_g h_g \mathbf{v}_g) =$$

$$= \epsilon_g \left(\frac{\partial p_g}{\partial t} + \mathbf{v}_g \cdot \nabla p_g \right) + \sum_{s=1}^{N} Q_s(T_s - T_g), \tag{6}$$

$$\frac{\partial(\epsilon_s \rho_s h_s)}{\partial t} + \nabla \cdot (\epsilon_s \rho_s h_s \mathbf{v}_s) = Q_s(T_g - T_s). \tag{7}$$

Here, Q_s is the volumetric heat transfer rate between the gas and the s-th solid phase. For the gas phase, we have considered the reversible rate of enthalpy change due to compression or expansion, which is important in transient, compressible flows. Heat transfer between different solid phases is negligible, and also radiative heat transfer has not been considered. As remarked before, viscous dissipation has been neglected for the applications considered in this paper, based on the results of the scale analysis.

By definition of the volumetric and mass fractions, one also has the relations

$$\epsilon_g + \sum_{s=1}^{N} \epsilon_s = 1, \quad 0 \le \epsilon_g \le 1, \quad 0 \le \epsilon_s \le 1,$$
$$\sum_{l=1}^{M} y_l = 1, \qquad 0 \le y_l \le 1. \tag{8}$$

The gas phase is compressible and we suppose that thermodynamic quantities are related by the ideal gas law:

$$p_g = \tilde{R}\rho_g T_g, \tag{9}$$

where $\tilde{R}$ is the gas constant of the mixture of gaseous components. Particulate solid phases are considered incompressible. Consequently, their microscopic density is assumed to be constant and denoted by ρ_s, $s = 1 \dots N$. The temperature of each phase is derived from its enthalpy as:

$$T_s = \frac{h_s}{c_{p,s}}, \quad s = g, 1 \dots N \tag{10}$$

where the constant pressure specific heats of the particles $c_{p,s}$ are assumed to be constant and to correspond to average values, due to their minor sensitivity on temperature. The specific heat of the gas phase $c_{p,g}$ depends on temperature and it is computed as a weighted average of the specific heats of the M chemical components:

$$c_{p,g} = \sum_{l=1}^{M} y_l c_{p,l}. \tag{11}$$

Interphase drag coefficients and heat transfer rates are derived from semi-empirical correlations for dilute and dense regimes and they are reported in Appendix B.

The initial values of all field variables must be specified for the entire computational domain. Usually, a standard atmosphere, vertically stratified in pressure, temperature and density, is considered throughout the domain. The atmosphere is composed of dry air at rest and no particle of any size is considered present in the computational domain. Appropriate boundary conditions will be defined later for each specific test case.

2 The numerical method: semi-implicit time discretization

The model equations described in the previous section are discretized in time by a second order version of the implicit multifield (IMF) algorithm proposed in Harlow and Amsden (1975). We will describe the time discretization method in the simpler case of a single solid phase s. We employ a semi-implicit time discretization based on a Crank-Nicolson type time averaging (also known as θ-method) with averaging parameter $\theta \in [0,1]$ (Crank and Nicolson, 1947). It is well known (see e.g. Quarteroni et al., 2002) that, for unconditional linear stability, one has to choose $\theta \geq 1/2$, while full second order accuracy is only granted for the limit value $\theta = 1/2$.

The continuity equations for the gas g and the solid phase s are discretized as:

$$
\begin{aligned}
(\epsilon_g \rho_g)^{n+1} + \theta \Delta t \left[\nabla \cdot (\epsilon_g \rho_g \mathbf{v}_g) \right]^{n+1} = \\
= (\epsilon_g \rho_g)^n - (1-\theta) \Delta t \left[\nabla \cdot (\epsilon_g \rho_g \mathbf{v}_g) \right]^n,
\end{aligned}
\tag{12}
$$

$$
\begin{aligned}
(\epsilon_s \rho_s)^{n+1} + \theta \Delta t \left[\nabla \cdot (\epsilon_s \rho_s \mathbf{v}_s) \right]^{n+1} = \\
= (\epsilon_s \rho_s)^n - (1-\theta) \Delta t \left[\nabla \cdot (\epsilon_s \rho_s \mathbf{v}_s) \right]^n.
\end{aligned}
\tag{13}
$$

The momentum equations for the gas g and the solid phase s are discretized as:

$$
\begin{aligned}
(\epsilon_g \rho_g \mathbf{v}_g)^{n+1} + \theta \Delta t \left[\epsilon_g \nabla p_g - D_{g,s}^n (\mathbf{v}_s - \mathbf{v}_g) - \epsilon_g \rho_g \mathbf{g} \right]^{n+1} = \\
= (\epsilon_g \rho_g \mathbf{v}_g)^n - \Delta t \left[\nabla \cdot (\epsilon_g \rho_g \mathbf{v}_g \mathbf{v}_g) \right]^n + \\
+ (1-\theta) \Delta t \left[-\epsilon_g \nabla p_g + D_{g,s}^n (\mathbf{v}_s - \mathbf{v}_g) + \epsilon_g \rho_g \mathbf{g} \right]^n,
\end{aligned}
\tag{14}
$$

$$
\begin{aligned}
(\epsilon_s \rho_s \mathbf{v}_s)^{n+1} + \theta \Delta t \left[\epsilon_s \nabla p_g - D_{g,s}^n (\mathbf{v}_g - \mathbf{v}_s) - \epsilon_s \rho_s \mathbf{g} \right]^{n+1} = \\
= (\epsilon_s \rho_s \mathbf{v}_s)^n - \Delta t \left[\nabla \cdot (\epsilon_s \rho_s \mathbf{v}_s \mathbf{v}_s) \right]^n + \\
+ (1-\theta) \Delta t \left[-\epsilon_s \nabla p_g + D_{g,s}^n (\mathbf{v}_g - \mathbf{v}_s) + \epsilon_s \rho_s \mathbf{g} \right]^n.
\end{aligned}
\tag{15}
$$

Notice that the pressure, the gravity and the drag terms are discretized in time by the θ-method, while all the other terms are treated explicitly. The enthalpy equations for the gas phase g and the solid phase s are discretized as:

$$
\begin{aligned}
\left(\epsilon_g \rho_g h_g\right)^{n+1} + \theta\Delta t\, Q_s^n \left[T_s - T_g\right]^{n+1} = \\
= (\epsilon_g \rho_g)^{n+1} h_g^n - (1-\theta)\Delta t\, Q_s^n \left[T_s - T_g\right]^n - \\
- \Delta t\, \left[\nabla \cdot \left(\epsilon_g^{n+1} \rho_g^{n+1} h_g^n \mathbf{v}_g^{n+1}\right)\right] + \\
+ \Delta t\, \left[\epsilon_g^{n+1}\left(\frac{p_g^{n+1} - p_g^n}{\Delta t} + \mathbf{v}_g^{n+1} \cdot \nabla p_g^{n+1}\right)\right],
\end{aligned} \qquad (16)
$$

$$
\begin{aligned}
(\epsilon_s \rho_s h_s)^{n+1} + \theta\Delta t\, Q_s^n \left[T_s - T_g\right]^{n+1} = \\
= (\epsilon_s \rho_s)^{n+1} h_s^n - (1-\theta)\Delta t\, Q_s^n \left[T_s - T_g\right]^n - \\
- \Delta t\, \left[\nabla \cdot \left(\epsilon_s^{n+1} \rho_s^{n+1} h_s^n \mathbf{v}_s^{n+1}\right)\right].
\end{aligned} \qquad (17)
$$

Only the interphase exchange term is treated semi-implicitly by the θ-method, while all the other terms are treated explicitly, assuming that the continuity and momentum equations have been solved already. The previous equations can be reformulated as

$$
\begin{aligned}
(\epsilon_g \rho_g)^{n+1} + \theta\Delta t\, \left[\nabla \cdot (\epsilon_g \rho_g \mathbf{v}_g)\right]^{n+1} &= \mathcal{E}_{\rho_g}^n, \\
(\epsilon_s \rho_s)^{n+1} + \theta\Delta t\, \left[\nabla \cdot (\epsilon_s \rho_s \mathbf{v}_s)\right]^{n+1} &= \mathcal{E}_{\rho_s}^n, \\
(\epsilon_g \rho_g \mathbf{v}_g)^{n+1} + \theta\Delta t\, \left[\epsilon_g \nabla p_g - D_{g,s}^n\left(\mathbf{v}_s - \mathbf{v}_g\right) - \epsilon_g \rho_g \mathbf{g}\right]^{n+1} &= \mathcal{E}_{\mathbf{v}_g}^n, \\
(\epsilon_s \rho_s \mathbf{v}_s)^{n+1} + \theta\Delta t\, \left[\epsilon_s \nabla p_g - D_{g,s}^n\left(\mathbf{v}_g - \mathbf{v}_s\right) - \epsilon_s \rho_s \mathbf{g}\right]^{n+1} &= \mathcal{E}_{\mathbf{v}_s}^n, \\
(\epsilon_g \rho_s h_g)^{n+1} - \theta\Delta t\, Q_s^n\left[T_s - T_g\right]^{n+1} &= \mathcal{E}_{h_g}^n, \\
(\epsilon_s \rho_s h_s)^{n+1} - \theta\Delta t\, Q_s^n\left[T_g - T_s\right]^{n+1} &= \mathcal{E}_{h_s}^n,
\end{aligned}
$$
$$(18)$$

where the $\mathcal{E}$ terms include all the explicit terms.

For each time step t^{n+1}, equations (12)-(17) are solved by this second order extension of the IMF algorithm as follows:

- temperature dependent coefficients of the gas phase are computed;

- the interphase coefficients D_{sp} and Q_s and the explicit $\mathcal{E}$ terms are computed;

- the coupled continuity and momentum equations are solved iteratively to update velocity fields, pressure and volumetric fractions;

10

- gas mass fractions y_l are computed by solving the linear transport equations;

- the energy equations are solved explicitly for all phases (the system is linear in the temperatures).

We can observe that, since the enthalpy equations are solved explicitly after the solution of the momentum and continuity equations, the temperature is kept constant during the solution procedure. The effect of the temperature variation on the gas pressure and density are deferred to the next time-step computation.

3   The numerical method: space discretization

A staggered discretization grid with at most $N_x \times N_y \times N_z$ computational cells is introduced, along the lines of popular discretization methods such as the MAC (marker and cell) approach, introduced in Harlow and Welch (1965), or the Arakawa C grid (see e.g. Arakawa and Lamb, 1981). Each cell is numbered at its center with indices i, j and k, for the x, y and z directions, respectively. The length of the cell sides in each directions are denoted by Δx_i, Δy_j and Δz_k and they are assumed to vary in their respective direction only. The cell volume is given by $V_{i,j,k} = \Delta x_i \Delta y_j \Delta z_k$ and staggered spacings $\Delta x_{i+\frac{1}{2}}$ are defined as the arithmetic average of the neighboring, integer index values.

The discrete u velocity is defined at half integer i and integers j and k, v is defined at integers i, k and half integer j, while w is defined at integers i, j and half integers k. Finally, p and all other three-dimensional scalar variables are defined at integers i, j, k. At points where they are not defined, the discrete variables are generally computed by simple arithmetical mean of the nearest defined values. Averaged quantities will usually be denoted by an overbar. On a uniform grid, for example:

$$\bar{u}_{i,j,k} = \frac{u_{i+\frac{1}{2},j,k} + u_{i-\frac{1}{2},j,k}}{2},$$

$$\bar{u}_{i,j+\frac{1}{2},k} = \frac{u_{i+\frac{1}{2},j,k} + u_{i-\frac{1}{2},j,k} + u_{i+\frac{1}{2},j+1,k} + u_{i-\frac{1}{2},j+1,k}}{4}.$$

The model equations are discretized by a finite volume approach on an orthogonal, non uniform mesh. The mesh is composed by rectangular control volumes obtained from the cartesian product of three 1D discretization intervals along each axis. If we denote by
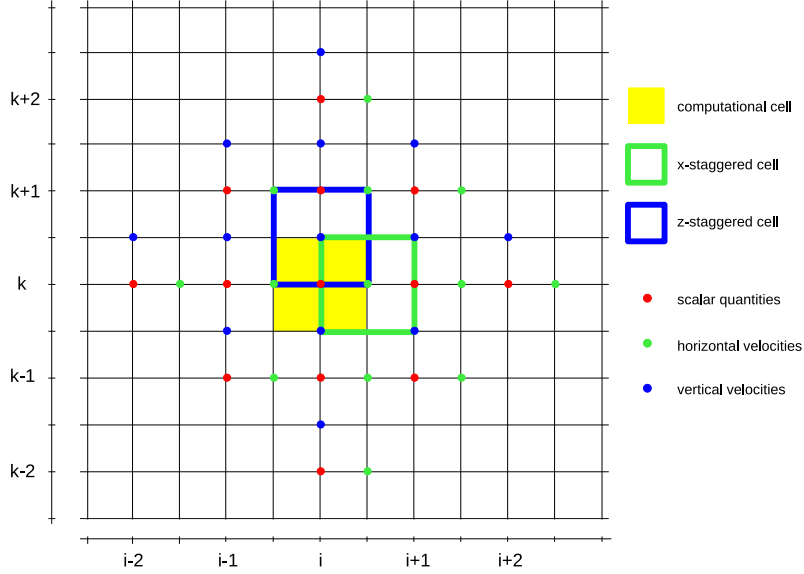
Figure 1: Sketch of the 2D computational stencil of the cell (i, k).

$i = 1 \ldots N_x$, $j = 1 \ldots N_y$, $k = 1 \ldots N_z$ the intervals along the x, y and z axis, respectively, the center of each cell can be identified by a triplet of indices (i, j, k). The scalar quantities that appear in the transport equations, i.e. pressure, densities, volumetric fractions and enthalpies, are defined at the cell centers, whereas the vectors, i.e. velocities, are defined at the C-grid staggered locations. Therefore mass and enthalpy equations are solved on the cell centers, whereas the momentum equations are solved at the staggered locations. In Figure 1, the 2D computational stencil of the cell (i, k) is sketched, including the neighbouring cells needed to reconstruct the fluxes through the cell boundaries. The structure of the stencil is related to the flux reconstruction technique that will be discussed later.

If we denote with brackets $\langle \ldots \rangle$ the discretization of the advective fluxes and we adopt the staggered approach described above, we obtain, for both the gas phase and the solid phase, for each cell (i, j, k) of the mesh, the following system of discretized equations:

12

$$(\epsilon_s \rho_s)_{ijk}^{n+1} + \theta \left[\frac{\Delta t}{\Delta x} \langle \epsilon_s \rho_s \bar{u}_s \rangle_{ijk}^{n+1} + \frac{\Delta t}{\Delta y} \langle \epsilon_s \rho_s \bar{v}_s \rangle_{ijk}^{n+1} + \frac{\Delta t}{\Delta z} \langle \epsilon_s \rho_s \bar{w}_s \rangle_{ijk}^{n+1} \right] = \mathcal{E}_{\rho_s,ijk}^n,$$

$$(\bar{\epsilon}_s \bar{\rho}_s u_s)_{i+\frac{1}{2}jk}^{n+1} + \theta \frac{\Delta t}{\Delta x} \bar{\epsilon}_{s,i+\frac{1}{2}jk}^{n+1} \left(p_{g,i+1jk}^{n+1} - p_{g,ijk}^{n+1} \right) -$$

$$-\theta \Delta t \, D_{ps,i+\frac{1}{2}jk}^n \left(u_{p,i+\frac{1}{2}jk}^{n+1} - u_{s,i+\frac{1}{2}jk}^{n+1} \right) - \theta \Delta t \, [\bar{\epsilon}_s \bar{\rho}_s g_x]_{i+\frac{1}{2}jk}^{n+1} = \mathcal{E}_{u_s,i+\frac{1}{2}jk}^n,$$

$$(\bar{\epsilon}_s \bar{\rho}_s v_s)_{ij+\frac{1}{2}k}^{n+1} + \theta \frac{\Delta t}{\Delta y} \bar{\epsilon}_{s,ij+\frac{1}{2}k}^{n+1} \left(p_{g,ij+1k}^{n+1} - p_{g,ijk}^{n+1} \right) -$$

$$-\theta \Delta t \, D_{ps,ij+\frac{1}{2}k}^n \left(v_{p,ij+\frac{1}{2}k}^{n+1} - v_{s,ij+\frac{1}{2}k}^{n+1} \right) - \theta \Delta t \, [\bar{\epsilon}_s \bar{\rho}_s g_y]_{ij+\frac{1}{2}k}^{n+1} = \mathcal{E}_{v_s,ij+\frac{1}{2}k}^n,$$

$$(\bar{\epsilon}_s \bar{\rho}_s w_s)_{ijk+\frac{1}{2}}^{n+1} + \theta \frac{\Delta t}{\Delta z} \bar{\epsilon}_{s,ijk+\frac{1}{2}}^{n+1} \left(p_{g,ijk+1}^{n+1} - p_{g,ijk}^{n+1} \right) -$$

$$-\theta \Delta t \, D_{ps,ijk+\frac{1}{2}}^n \left(w_{p,ijk+\frac{1}{2}}^{n+1} - w_{s,ijk+\frac{1}{2}}^{n+1} \right) - \theta \Delta t \, [\bar{\epsilon}_s \bar{\rho}_s g_z]_{ijk+\frac{1}{2}}^{n+1} = \mathcal{E}_{w_s,ijk+\frac{1}{2}}^n,$$

$$(\epsilon_s \rho_s h_s)_{ijk}^{n+1} - \theta \Delta t \, Q_{s,ijk}^n [T_s - T_g]_{ijk}^{n+1} = \mathcal{E}_{h_s,ijk}^n,$$

$$(19)$$

for all $s = g, 1 \ldots N$, where the discretization of the $\mathcal{E}$-terms has to be specified. The $\mathcal{E}$-terms are computed explicitly before the resolution of the system.

The expressions of the discrete $\mathcal{E}$-terms of the momentum equations are the following, for both the gas and the solid phase:

$$\begin{aligned}
\mathcal{E}_{u_s,i+\frac{1}{2}jk}^n = & \; (\bar{\epsilon}_s \bar{\rho}_s u_s)_{i+\frac{1}{2}jk}^n - \\
& -(1-\theta)\frac{\Delta t}{\Delta x} \bar{\epsilon}_{s,i+\frac{1}{2}jk}^n \left(p_{g,i+1jk}^n - p_{g,ijk}^n \right) + \\
& +(1-\theta)\Delta t \, D_{ps,i+\frac{1}{2}jk}^n \left(u_{p,i+\frac{1}{2}jk}^n - u_{s,i+\frac{1}{2}jk}^{n+1} \right) + \\
& +(1-\theta)\Delta t \, (\bar{\epsilon}_s \bar{\rho}_s g_x)_{i+\frac{1}{2}jk}^n - \frac{\Delta t}{\Delta x} \langle \bar{\epsilon}_s \bar{\rho}_s u_s^2 \rangle_{i+\frac{1}{2}jk}^n - \\
& -\frac{\Delta t}{\Delta y} \langle \bar{\epsilon}_s \bar{\rho}_s u_s \bar{v}_s \rangle_{i+\frac{1}{2}jk}^n - \frac{\Delta t}{\Delta z} \langle \bar{\epsilon}_s \bar{\rho}_s u_s \bar{w}_s \rangle_{i+\frac{1}{2}jk}^n,
\end{aligned}$$

$$(20)$$

13

$$
\begin{aligned}
\mathcal{E}^n_{v_s,ij+\frac{1}{2}k} =\ & (\bar{\epsilon}_s\bar{\rho}_s v_s)^n_{ij+\frac{1}{2}k} - \\
& -(1-\theta)\frac{\Delta t}{\Delta y}\,\bar{\epsilon}^n_{s,ij+\frac{1}{2}k}\left(p^n_{g,ij+1k} - p^n_{g,ijk}\right) + \\
& +(1-\theta)\Delta t\,D^n_{ps,ij+\frac{1}{2}k}\left(v^n_{p,ij+\frac{1}{2}k} - v^n_{s,ij+\frac{1}{2}k}\right) + \\
& +(1-\theta)\Delta t\,(\bar{\epsilon}_s\bar{\rho}_s g_y)^n_{ij+\frac{1}{2}k} - \frac{\Delta t}{\Delta x}\langle\bar{\epsilon}_s\bar{\rho}_s v_s\bar{u}_s\rangle^n_{ij+\frac{1}{2}k} - \\
& -\frac{\Delta t}{\Delta y}\langle\bar{\epsilon}_s\bar{\rho}_s v_s^2\rangle^n_{ij+\frac{1}{2}k} - \frac{\Delta t}{\Delta z}\langle\bar{\epsilon}_s\bar{\rho}_s v_s\bar{w}_s\rangle^n_{ij+\frac{1}{2}k},
\end{aligned}
\tag{21}
$$

$$
\begin{aligned}
\mathcal{E}^n_{w_s,ijk+\frac{1}{2}} =\ & (\bar{\epsilon}_s\bar{\rho}_s w_s)^n_{ijk+\frac{1}{2}} - \\
& -(1-\theta)\frac{\Delta t}{\Delta z}\,\bar{\epsilon}^n_{s,ijk+\frac{1}{2}}\left(p^n_{g,ijk+1} - p^n_{g,ijk}\right) + \\
& +(1-\theta)\Delta t\,D^n_{ps,ijk+\frac{1}{2}}\left(w^n_{p,ijk+\frac{1}{2}} - w^n_{s,ijk+\frac{1}{2}}\right) + \\
& +(1-\theta)\Delta t\,(\bar{\epsilon}_s\bar{\rho}_s g_z)^n_{ijk+\frac{1}{2}} - \frac{\Delta t}{\Delta x}\langle\bar{\epsilon}_s\bar{\rho}_s w_s\bar{u}_s\rangle^n_{ijk+\frac{1}{2}} - \\
& -\frac{\Delta t}{\Delta y}\langle\bar{\epsilon}_s\bar{\rho}_s w_s\bar{v}_s\rangle^n_{ijk+\frac{1}{2}} - \frac{\Delta t}{\Delta z}\langle\bar{\epsilon}_s\bar{\rho}_s w_s^2\rangle^n_{ijk+\frac{1}{2}}.
\end{aligned}
\tag{22}
$$

The expressions of the discrete $\mathcal{E}$-terms of the energy equations of the gas and the solid phase are the following:

$$
\begin{aligned}
\mathcal{E}^n_{h_g,ijk} =\ & (\epsilon_g\rho_g h_g)^n_{ijk} + \\
& +(1-\theta)\Delta t\,Q^n_{s,ijk}\,(T_s - T_g)^n_{ijk} - \\
& -\frac{\Delta t}{\Delta x}\langle\epsilon_g\rho_g h^n_g\bar{u}_g\rangle^{n+1}_{ijk} - \frac{\Delta t}{\Delta y}\langle\epsilon_g\rho_g h^n_g\bar{v}_g\rangle^{n+1}_{ijk} - \\
& -\frac{\Delta t}{\Delta z}\langle\epsilon_g\rho_g h^n_g\bar{w}_g\rangle^{n+1}_{ijk} + \epsilon^{n+1}_{g,ijk}\left(p^{n+1}_{g,ijk} - p^n_{g,ijk}\right) + \\
& +\frac{\Delta t}{\Delta x}(\bar{u}_g\epsilon_g)^{n+1}_{ijk}\left(\bar{p}^{n+1}_{g,i+\frac{1}{2}jk} - \bar{p}^{n+1}_{g,i-\frac{1}{2}jk}\right) + \\
& +\frac{\Delta t}{\Delta y}(\bar{v}_g\epsilon_g)^{n+1}_{ijk}\left(\bar{p}^{n+1}_{g,ij+\frac{1}{2}k} - \bar{p}^{n+1}_{g,ij-\frac{1}{2}k}\right) + \\
& +\frac{\Delta t}{\Delta z}(\bar{w}_g\epsilon_g)^{n+1}_{ijk}\left(\bar{p}^{n+1}_{g,ijk+\frac{1}{2}} - \bar{p}^{n+1}_{g,ijk-\frac{1}{2}}\right),
\end{aligned}
\tag{23}
$$

$$
\begin{aligned}
\mathcal{E}^n_{h_s,ijk} =\ & (\epsilon_s\rho_s h_s)^n_{ijk} + \\
& +(1-\theta)\Delta t\,Q^n_{s,ijk}\,(T_g - T_s)^n_{ijk} - \frac{\Delta t}{\Delta x}\langle\epsilon_s\rho_s h^n_s\bar{u}_s\rangle^{n+1}_{ijk} - \\
& -\frac{\Delta t}{\Delta y}\langle\epsilon_s\rho_s h^n_s\bar{v}_s\rangle^{n+1}_{ijk} - \frac{\Delta t}{\Delta z}\langle\epsilon_s\rho_s h^n_s\bar{w}_s\rangle^{n+1}_{ijk}.
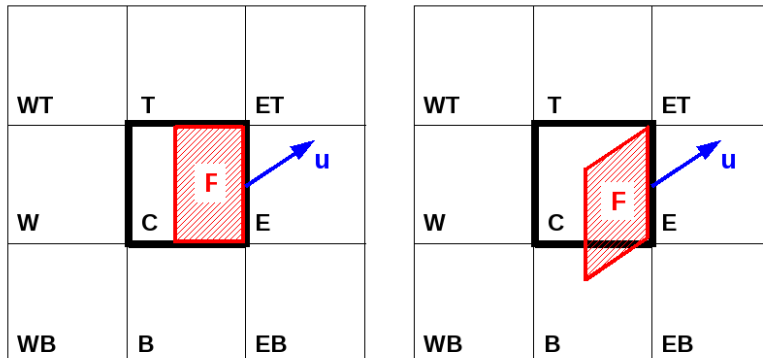\end{aligned}
\tag{24}
$$

Figure 2: Sketch of the computation of the upwind flux (left) and the Corner Transport Upwind flux (right). The upwind flux is computed using only the velocity component normal to the face, defined in the staggered location, whereas the Corner Transport Upwind flux is computed using the unsplit velocity, computed with an appropriate interpolation.

Finally, it is necessary to introduce an appropriate discretization technique for the advective fluxes. From the dimensional analysis we have seen that advection is one of the dominating phenomena in the process, so we expect that a proper numerical treatment of the advection terms should be necessary in order to obtain an accurate numerical solution. Therefore, a first possible modification of the donor-cell scheme is to introduce in the upwind discretization the so-called transverse fluxes (Colella, 1990; Saltzman, 1993; LeVeque, 1996). In the standard donor-cell upwind method, the advective flux through one single cell boundary is split into independent fluxes along the x-, y- and z-directions by using the velocities u, v and w in the directions normal to each interface. More accurate methods can be obtained by considering the flux with the proper speed $\mathbf{u} = (u, v, w)$, without splitting it along the three space directions (Figure 2). Unsplit upwind schemes are more accurate (in particular, less diffusive) and more stable than the original donor-cell upwind method.

This improved version of the upwind method is called the Corner Transport Upwind (CTU) method (Colella, 1990). A hierarchy of methods for the numerical solution of advective transport in conservation equations in several space dimensions based on CTU has been proposed by LeVeque (1996). In the present model, we employ one of the second order versions of the algorithm described in LeVeque (1996), including *minmod* flux limiting (Roe, 1986) to avoid the creation of spurious extrema in the solution.

15

4 Model validation: axisymmetric underexpanded jet

The proposed numerical method has been tested on two- and three-dimensional simulations of underexpanded jets and the numerical results obtained have been compared with both experimental and numerical results available in the literature. In order to simulate a cylindrical underexpanded jet, we assume that each phase enters the domain through a fixed inlet where the volume fraction, velocity and temperature of each phase and the gas pressure are imposed. Mechanical and thermal equilibrium between the phases at the vent are assumed. In two-dimensional tests, we solve the model equations in cylindrical coordinates and we impose symmetry conditions at the left lateral boundary (Figure 3). At the bottom boundary, no mass and heat transfer are allowed and free-slip conditions are assumed for the velocity of each phase. At the upper boundary, free outflow/inflow conditions are assumed, whereas at the lateral boundaries it is possible to assume either free-slip or free outflow/inflow conditions. In particular, at the outflow boundaries, the mass and momentum equations of the mixture are solved for pressure, assuming a null velocity gradient along the boundary. At the lateral inflow boundaries, incoming air is assumed to be free of particles and to have pressure and temperature characteristics corresponding to those of the standard reference atmosphere.
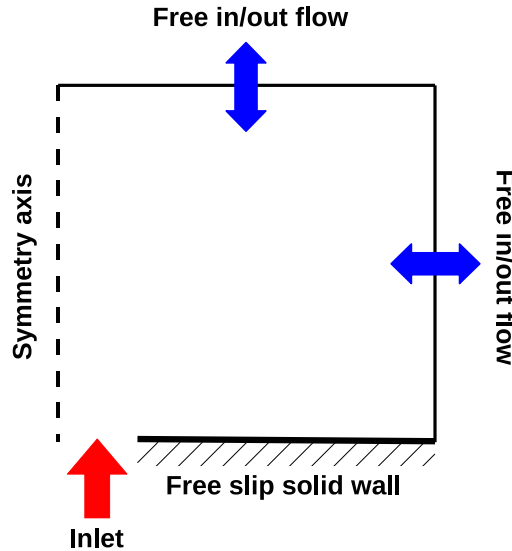

Figure 3: Boundary conditions for the jet test-case.

4.1 Comparison with laboratory results and empirical laws

We present here a set of numerical tests aimed at the simulation of a gas jet at the laboratory scale. It has been proven theoretically and experimentally that vents with supersonic vertical velocity and gas pressure greater than the atmospheric one result in a rapid expansion and acceleration of the fluid to high Mach numbers, e.g. Lewis and Carlson (1964) and Orescanin et al. (2010). A series of expansion waves form at the vent exit (Prandtl-Meyer expansion), which are reflected as compression waves at the jet flow boundary. The compression waves coalesce to form a barrel shock and a standing normal shock wave (Mach disk), across which the vertical velocity is reduced and the pressure in the core of the jet increases. The fluid that crosses the Mack disk is rapidly compressed and decelerated to subsonic speeds. Above the Mach disk, the fluid moves slowly in the core of the jet and it is surrounded by a supersonic moving shell, with a slip line or a shear layer dividing these regions (Figure 4).
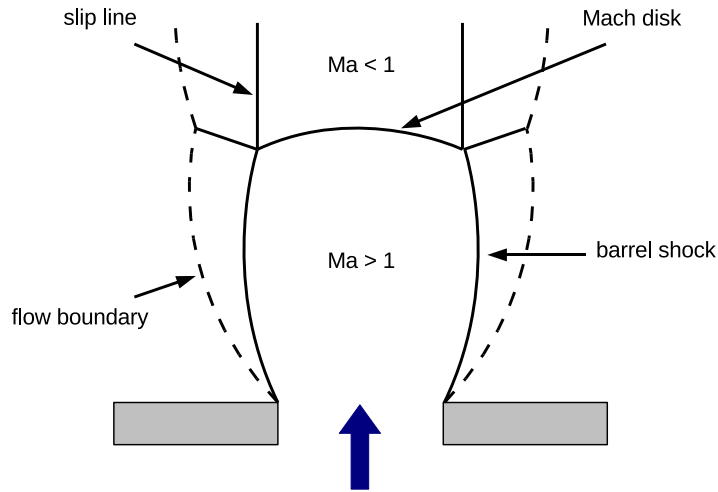

Figure 4: Decompression structure in underexpanded supersonic jets.

One of the important parameters describing these supersonic jets is the distance between the vent and the normal shock wave. Experimental results reported in Lewis and Carlson (1964) show that the height of the Mach disk h_d depends on the vent diameter

D_v, the exit Mach number Ma_v, the ratio of specific heats γ and the ratio K of the exit static pressure P_v and the atmospheric pressure P_{atm}. The empirical relationship is

$$h_d = 0.69 D_v Ma_v \sqrt{\gamma K}.$$

We consider an homogeneous fluid (dry air with standard chemical components), and we impose underexpanded sonic or supersonic conditions at the inlet (Table 1), i.e., the gas pressure at the inlet is larger than the atmospheric and the Mach number ($Ma = |\mathbf{u}|/c$, where c is the speed of sound in the mixture, see Appendix A) is larger or equal than 1. The computational domain is a box of size 0.1×0.2 m, whose left side coincides with the axis of the vent. The side and the bottom boundaries of the axisymmetric domain are impermeable and stress free. Two uniform meshes of 160×320 ($\Delta x = \Delta z = 6.25 \cdot 10^{-4}$ m) and 500×1000 ($\Delta x = \Delta z = 2 \cdot 10^{-4}$ m) cells have been employed, with time steps of $\Delta t = 10^{-7}$ s and $\Delta t = 5 \cdot 10^{-8}$ s, respectively. We consider different values of overpressure levels K and we evaluate the height of the Mach disk h_d.

We obtain a good agreement between experimental results and numerical simulations (Figure 5). In Figures 6 and 7, the results obtained in terms of vertical velocity and temperature are shown. The improved version of the PDAC code have a better fit with experimental results and is able to describe the shear layer instability above the Mach disk. In general, the first order version of the model tends to underestimate the Mach disk height. Moreover, for small values of overpressure K, using first order methods we do not see the formation of the Mach disk, whereas the second order method is able to capture the sharp discontinuity in the flow (Figure 8).

Vent conditions		
D_v	[m]	0.01
$K = p_v/p_{atm}$		2, 5, 10, 20
w_v	[m/s]	346
T_v	[K]	298
Ma_v		1.0

Table 1: Inlet conditions for a homogeneous underexpanded jet at the laboratory scale.
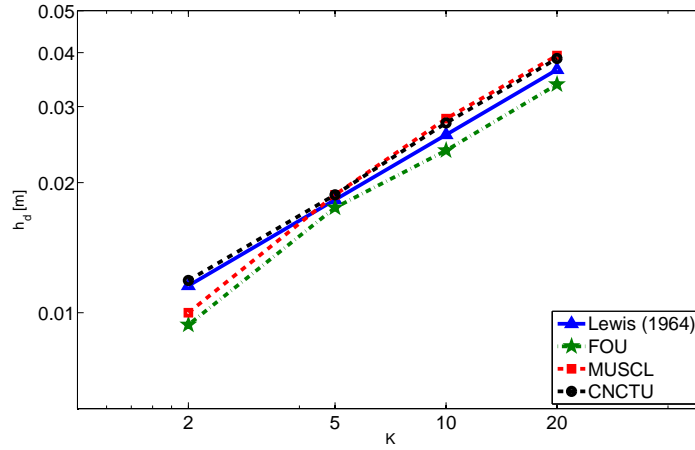
Figure 5: Comparison between experimental and numerical results in terms of Mach disk height for different values of the vent overpressure K. The results in Lewis and Carlson (1964) are compared with numerical simulation applying first order donor-cell upwind method (FOU), upwind method with second order MUSCL fluxes (MUSCL) and second order Corner Transport Upwind method with θ-method time discretization (CNCTU).
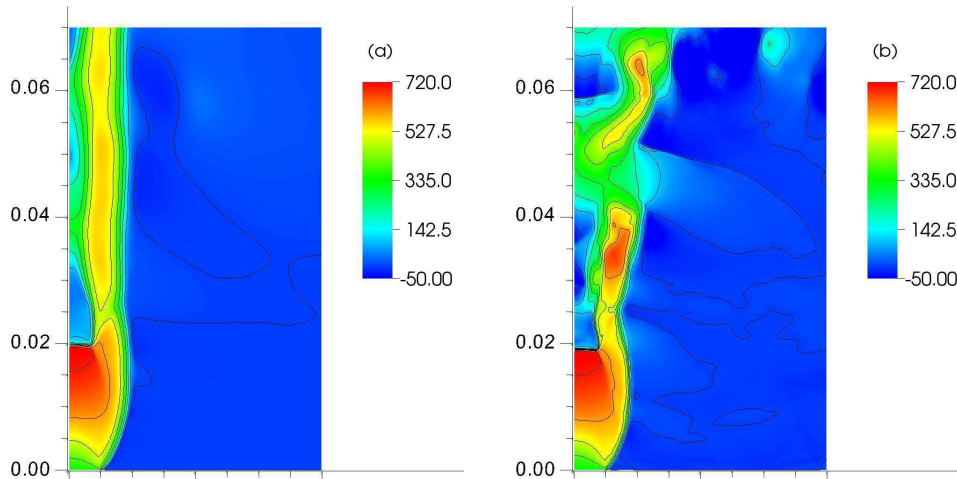

Figure 6: Vertical velocity. Isolines [0:100:700] m/s. Comparison between (a) first order upwind method FOU and (b) second order method CNCTU with $K = 5$ on a 500×1000 mesh.

19
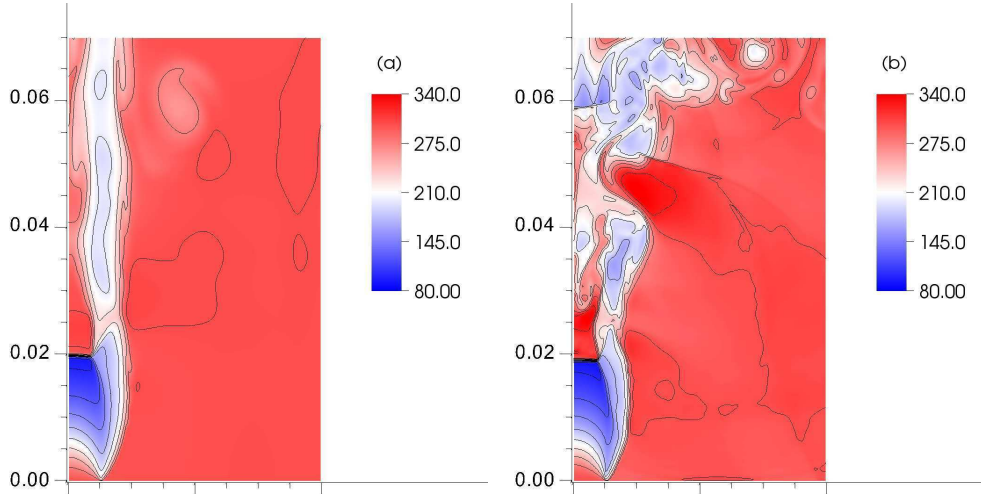
Figure 7: Temperature. Isolines [50:25:350] K. Comparison between (a) first order upwind method FOU and (b) second order method CNCTU with $K = 5$ on a 500×1000 mesh.
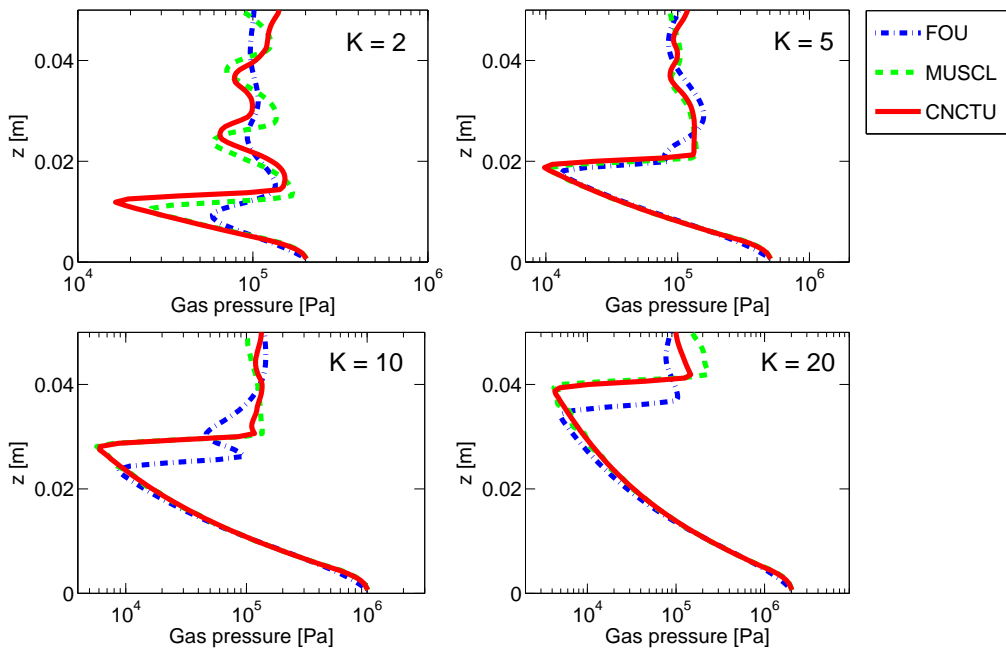

Figure 8: Gas pressure. Axial profile for different values of the vent overpressure K computed on a coarse mesh. Comparison between first order (FOU) and second order methods (MUSCL and CNCTU) on a 160×320 mesh.

4.2 Comparison with pseudogas simulations

To investigate the dynamics of underexpanded particle-laden jets, we have performed a set of simulations with inlet conditions corresponding to those analyzed by Ogden et al. (2008b). These simulations are performed in absence of gravity, in order to focus on compressibility and non-equilibrium multiphase effects. We assume choked flow conditions at the vent (i.e., the inflow velocity is equal to the speed of sound of the mixture and $Ma_v = 1$). As in the previous benchmark, the side and the bottom boundaries of the axisymmetric two-dimensional domain are impermeable and stress-free.

Inlet conditions for numerical simulations are specified in Table 2. The mixture is composed by water vapor and solid particles that are injected in a standard atmosphere composed by dry air. In order to facilitate the comparison with the result obtained with the equilibrium, pseudogas model, we first consider a single, fine solid phase with particle diameter equal to 10 μm, which is tightly coupled to the gas phase. Two different inlet pressure ratios of $K = 20$ (Case A) and $K = 5$ (Case B) were adopted. A third run (Case C) is performed with $K = 5$ and a mixture of particles of 10 μm and 1000 μm.

In Case A, the computational domain is a box of size 800×2400 m and we use a uniform 200×600 mesh, with $\Delta x = \Delta z = 4$ m and a time step $\Delta t = 10^{-4}$ s. Figure 9 shows the vertical velocity field of the gas phase and the particle distribution above the vent after 20 seconds, when steady state conditions are reached. The simulation reproduces the expected behaviour of a supersonic underexpanded jet, displaying the barrel shock with a convex Mach disk, at about 320 m above the vent, which decelerates the mixture down to subsonic velocities (Figure 9a) and compresses the gas phase, so that the particle volumetric fraction increases by one order of magnitude across the discontinuity (Figure 9b).

To better analyze the jet dynamics and to quantitatively compare our results with those of Ogden et al. (2008b), we study the time-averaged vertical profiles along the axis of pressure, mixture density, gas vertical velocity and gas temperature, shown in Figure 10. The gas phase undergoes a rapid expansion from the initial pressure of $2.02 \cdot 10^6$ Pa to pressure values below atmospheric pressure. The minimum of the pressure is $9.1 \cdot 10^3$ Pa and it is reached at the height of 324 m from the vent. The ratio between Mach disk height and vent radius is 8.1 and the difference with respect to the corresponding result of Ogden et al. (2008b) is around 1%. Through the normal compression shock, the gas phase returns to atmospheric values. During the expansion, as expected in supersonic

flows, the gas phase accelerates up to 482 m/s and then through the shock it abruptly decelerates to a subsonic turbulent regime, with a vertical velocity around 33 m/s. During the expansion and acceleration phase, the gas decreases its temperature down to 1104 K and then warms up again by about 70 K through the Mach disk. Mixture density, defined as $\rho_m = \epsilon_g \rho_g + \epsilon_s \rho_s$, decreases by two orders of magnitude above the vent and then it increases of one order of magnitude through the shock. The difference in the Mach disk position with respect to the results reported in Ogden et al. (2008b) is around 4%, whereas the difference in the maximum vertical velocity is around 2%.

In Case B we consider an inlet pressure ratio of $K = 5$ and a vent diameter of 20 m (Table 2) in order to maintain the sonic conditions at the vent. The computational domain is a box of size 200×400 m and we use a uniform 200×1000 mesh, with $\Delta x = 1$ m, $\Delta z = 0.4$ m and a time step $\Delta t = 5 \cdot 10^{-5}$ s. Figure 11 shows the gas vertical velocity and the particle volume fraction when the steady state configuration of the normal shock is achieved. The two-dimensional jet pattern and shape closely fit the results presented in Figure 3b by Ogden et al. (2008b). The results obtained with the multiphase model are thus in quantitative agreement with the result obtained by Ogden et al. (2008b), demonstrating that the pseudogas approximation is acceptable in the underexpanded jet regime, at least for fine particles.

Finally, in Case C we consider the same configuration as in Case B and we change the gas and particle mixture by introducing a second class of solid particles with diameter equal to 1000 μm. The vertical, axial profiles of Case B and C, displayed in Figure 12, report a Mach disk height around 39 m from the vent and the ratio between the Mach disk height and the vent radius is 3.9, in agreement with the numerical and experimental results reported in Ogden et al. (2008b). In Case B, the maximum vertical velocity of the gas phase is 413 m/s while the minimum temperature along the axis is 1132 K, showing a temperature decrease of about 5%, in reason of the higher heat capacity of particles. In Case C, the Mach disk position is unchanged, whereas we observe a peak velocity about 30 m/s lower. Above the normal shock, gas velocity is 56 m/s in Case B and 87 m/s in Case C. Flow density is also considerably higher in Case C.

4.2.1 Assessment of multiphase effects

Non-equilibrium (kinetic and thermal) effects in multiphase flows are controlled by drag and energy exchange terms in the momentum

Vent conditions		Case A	Case B	Case C
D_v	[m]	80	20	20
K		20	5	5
w	[m/s]	150.3	150.3	150.3
T	[K]	1200	1200	1200
Ma_v		1.0	1.0	1.0
ϵ_{s_1}		0.08784	0.021985	0.010992
d_{s_1}	[μm]	10	10	10
ρ_{s_1}	[kg/m^3]	1000	1000	1000
ϵ_{s_2}		-	-	0.010992
d_{s_2}	[μm]	-	-	1000
ρ_{s_2}	[kg/m^3]	-	-	1000

Table 2: Inhomogeneous underexpanded jet.
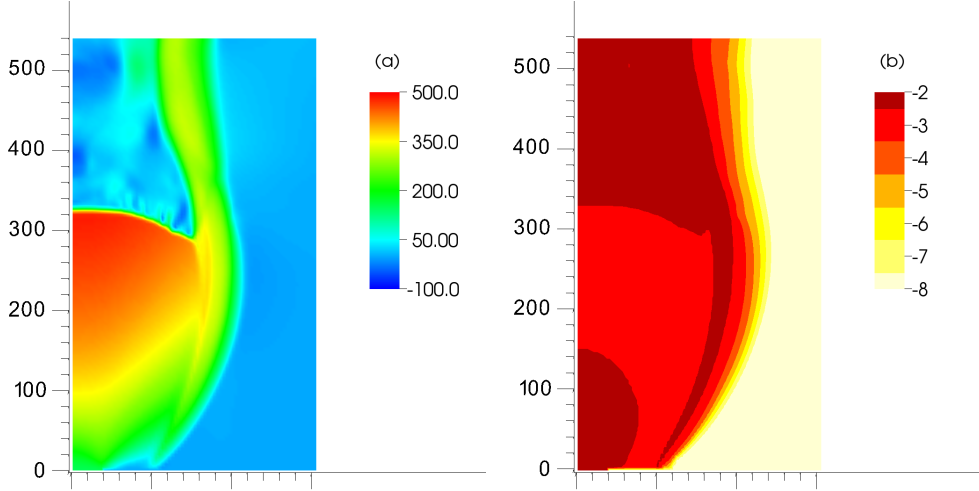
Figure 9: Case A. (a) Gas vertical velocity and (b) logarithm of particle volume fraction. Snapshots at $t = 20$ s.
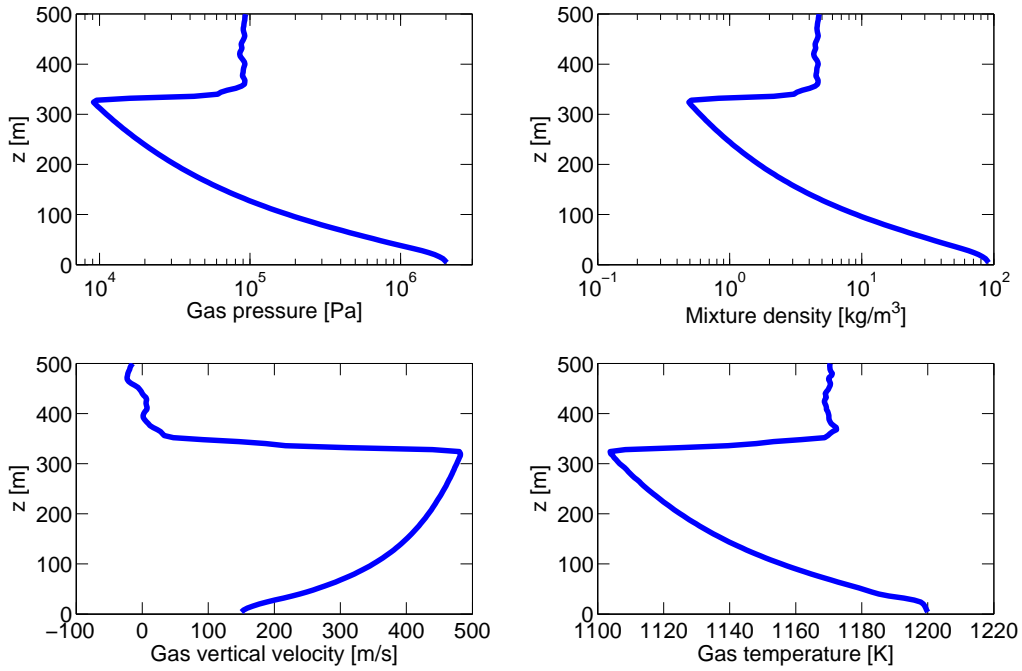
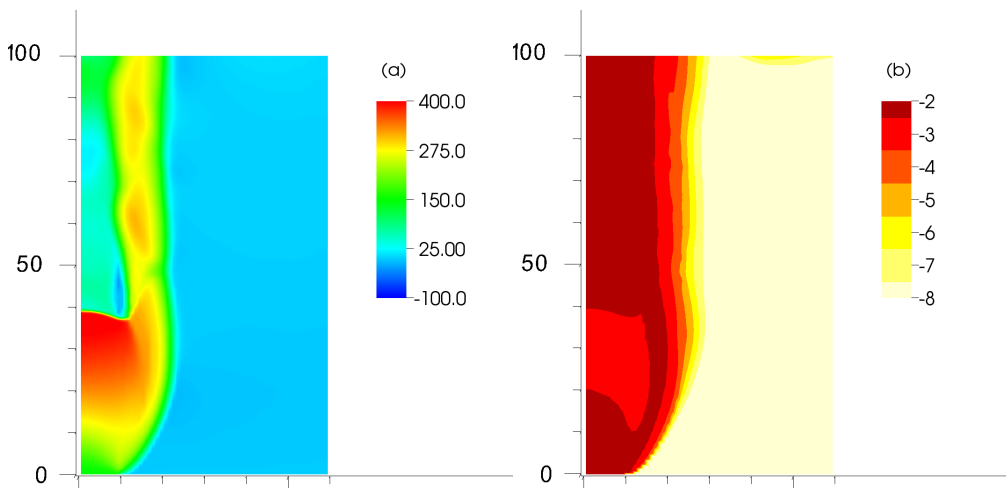Figure 10: Case A. Time-averaged axial profiles computed over the interval $[16, 20]$ s.

Figure 11: Case B. (a) Gas vertical velocity and (b) logarithm of particle volume fraction. Snapshots at $t = 2$ s.
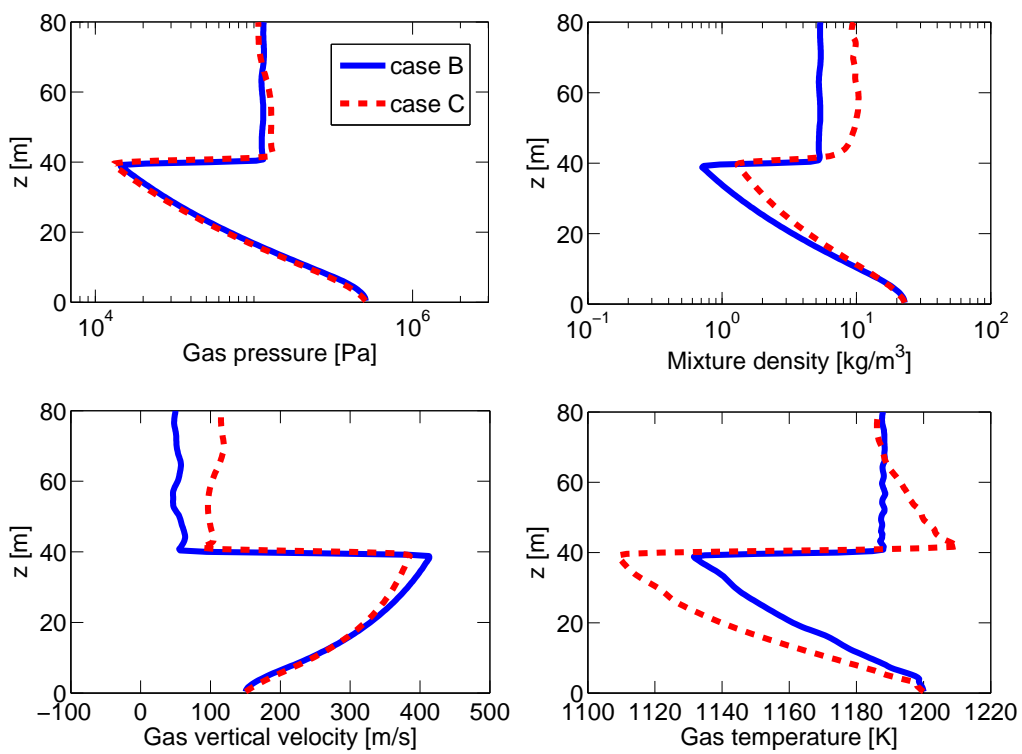
24

Figure 12: Case B and C. Time-averaged axial profiles computed over the interval $[1.6, 2.0]$ s.

and energy equations. Dilute gas-particle flow can be characterized by a time scale (the *particle relaxation time*) determined by the balance between particle inertia and viscous drag. Its expression can be derived from the momentum balance equation for the solid particles (Equation 5) by neglecting all the terms except the drag and inertial terms:

$$\frac{\partial(\epsilon_s \rho_s \mathbf{w}_s)}{\partial t} \simeq D_{g,s}(\mathbf{w}_g - \mathbf{w}_s). \tag{25}$$

The relaxation time is thus defined from Equation 25 as:

$$\tau_s = \frac{\epsilon_s \rho_s}{D_{g,s}}. \tag{26}$$

(a simple analysis, e.g. Marble (1970), suggests that the time scale for thermal relaxation has the same order of magnitude).

For dilute mixtures ($\epsilon_g \approx 1$) and low gas-particle Reynolds number (defined by Equation 32), the particle relaxation time approximates that of a single particle in a laminar flow

$$\tau_s \simeq \frac{\rho_s d_s^2}{18\mu_g}. \tag{27}$$

However, in general, the drag coefficient in Equation 26 is a complex function of the gas-particle Reynolds number and particle concentration. In the underexpanded jet, the flow is always in a dilute regime, with $\epsilon_g > 0.8$. In these conditions, the drag coefficient of Wen and Yu (1966) can be adopted and the relaxation time becomes

$$\tau_s \simeq \frac{\epsilon_s \rho_s}{D_{g,s}} = \frac{\epsilon_s \rho_s}{\frac{3}{4} C_{d,s} \frac{\epsilon_g \epsilon_s \rho_g |\mathbf{w}_g - \mathbf{w}_s|}{d_s} \epsilon_g^{-2.7}} \tag{28}$$

where the coefficient $C_{d,s}$ depends on the gas-particle Reynolds number Re_s (Equation 34).

The relaxation time τ_s gives an order of magnitude of the time delay with which a particle equilibrates to a time-varying gas flow. In a supersonic jet, such delay may occur in the rapid expansion region above the vent, where a difference between gas and particle velocity Δw may be expected. Across the normal shock, on the other hand, particles will equilibrate to the gas flow within a distance l, also known as shock relaxation (Marble, 1970).

To estimate the magnitude of the relaxation time, we first estimate from numerical results the maximum relative Reynolds number (Equation 32) in order to estimate the drag coefficient $D_{d,s}$. We assume that the maximum disequilibrium is achieved across

the Mach disk, where the gas phase is decelerated almost instantaneously while particles cross the discontinuity undisturbed before slowing down by the effect viscous drag. By using the gas velocity jump across the shock and the gas density after the shock, we estimate the maximum relative gas-particle Reynolds number of the order of 24 (Case A) and 19 (Case B). Therefore, in these cases we can use Equation 27 to estimate the particle relaxation time, obtaining $\tau_s = 1.5 \times 10^{-4}$ s (by assuming water vapor viscosity at 1000 K equal to $\mu_g = 3.7 \cdot 10^{-5}$ kg/m· s).

We can compare the particle relaxation time with the formation time of the Mach disk (Orescanin et al., 2010), that can be estimated as

$$\tau_{Ma} = \frac{D_v}{2c_{s,mix}}$$

where $c_{s,mix}$ is the mixture speed of sound, defined as:

$$c_{s,mix} = \sqrt{\tilde{R}T \frac{\rho_g}{\epsilon_g(\epsilon_g\rho_g + \epsilon_s\rho_s)}}. \tag{29}$$

(Pelanti and LeVeque, 2006).

Taking $T = 1000$ K and considering a dilute mixture of water vapor and solid particle with $\rho_s = 1000$ kg/m^3, $\epsilon_s = 0.01$, $\rho_g = 0.2$ kg/m^3, we obtain $c_{s,mix} \simeq 300$ m/s and in Case A $\tau_{Ma} \simeq 0.1$ s and in Case B $\tau_{Ma} \simeq 0.03$ s. Therefore both in Case A and Case B, the particle relaxation time is much smaller than the formation time of the Mach disk ($\tau_s \ll \tau_{Ma}$), thus meaning that fine particles dynamics is strongly coupled with the gas dynamics. Multiphase effects are negligible and the pseudogas approximation is valid.

In Case C, we can proceed in an analogous way, by assuming that coarse particles move in a fluid composed by water vapor plus fine particles in mechanical and thermal equilibrium, described as a pseudogas (as verified in Cases A and B). We can compute properties of the pseudogas ρ_{ps}, μ_{ps} and use them to carry out the relaxation time estimate for larger particles.

In the first 10 meters above the vent, small particles volume fraction decreases rapidly of one order of magnitude down to $5 \cdot 10^{-4}$ before the shock. The pseudogas density before the shock is $\rho_{ps} = \epsilon_g\rho_g + \epsilon_{s_1}\rho_{s_1} = 1.2$ kg/m^3. Its mean viscosity can be computed by using the Einstein's equation (Einstein, 1906) (which is valid for low concentrations) as $\mu_{ps} \simeq \mu_g(1 + 2.5\epsilon_{s_1}) = 3.71 \cdot 10^{-5}$ Pa·s, not very different from the value for pure water vapor. The maximum gas-particles Reynolds number, computed from the gas velocity jump across the shock $|w_g^b - w_g^a| = 298$ m/s, is $Re_s \simeq 9 \cdot 10^3$, thus implying that the low-Re approximation (Equation 27) for the relaxation time

is not applicable. In regimes where $Re_s > 1000$ we can estimate the relaxation time with the Reynolds number correction, as reported in Equation 34, that is

$$\tau_s \simeq \frac{\epsilon_{s_2}\rho_s}{D_{ps,s_2}} = \frac{\rho_{s_2}d_{s_2}^2}{0.33Re_{s_2}\mu_{ps}} \simeq 0.01 \, \text{s}.$$

In Case C the particle relaxation time and the formation time of the Mach disk are comparable, thus we investigate in detail the non-equilibrium effects for the coarsest particles on the underexpanded jet.

We first estimate the magnitude of the velocity difference between gas and particle below the shock as $\Delta w^{est} \approx a\tau_s w_g^b$, where $a = \frac{dw_g}{dz}$ is the gas velocity vertical gradient below the shock, and w_g^b is the vertical gas velocity below the shock. Based on the results discussed in the previous Section (Figures 10 and 12) a is taken as constant.

We can also derive a theoretical estimate of the relaxation distance above the shock as $l^{est} = |w_g^b - w_g^a| \cdot \tau_s$, where $|w_g^b - w_g^a|$ is the gas velocity jump across the normal shock.

In the expansion region, the velocity gradient a is approximatively equal to 6 s^{-1}, the gas velocity is $w_g^b = 386$ m/s, and we obtain $\Delta w_C^{est} \simeq 23$ m/s. Across the Mach disk, the jump in vertical gas velocity is 299 m/s. The distance to which particles equilibrate to the gas flow above the shock can be computed by assuming and initial disequilibrium velocity of the same order of magnitude and the relaxation time, obtaining $l_C^{est} \simeq |w_g^b - w_g^a| \cdot \tau_s \simeq 3$ m.

Figure 13 shows the differences between gas and particles velocity and temperature in Case C. We observe that smaller particles are essentially in thermal and mechanical equilibrium with the gas phase, as expected from theoretical results. Larger particles just below the normal shock are slower that the gas of about 25 m/s, they cross the shock with a vertical velocity that is about 140 m/s larger than the gas vertical velocity and finally they reach an equilibrium velocity close to the gas velocity. Larger particles tends to cool slower than the gas and the smaller particles and so their temperature is about 70 K higher than the gas temperature when they reach the Mach disk.

We therefore conclude that, for coarse particles, the significant difference observed in Figure 13 with respect to the fine particles is associated to the larger relaxation time of coarse particles. The gas shock is resolved through 5 computational cells, so that the velocity jump is, in practice, less steep than assumed. The theoretical relaxation length is comparable to the vertical grid size, so that nu-

merical resolution appear adequate to quantitatively resolve shock relaxation. In particular, after the normal shock, particles slow down to the gas velocity within 6 computational cells, from 40.4 m to 42.8 m. The numerical estimate of the relaxation distance $l_C \simeq 2.4$ m is thus comparable with the theoretical one $l_C^{est} \simeq 3$ m.
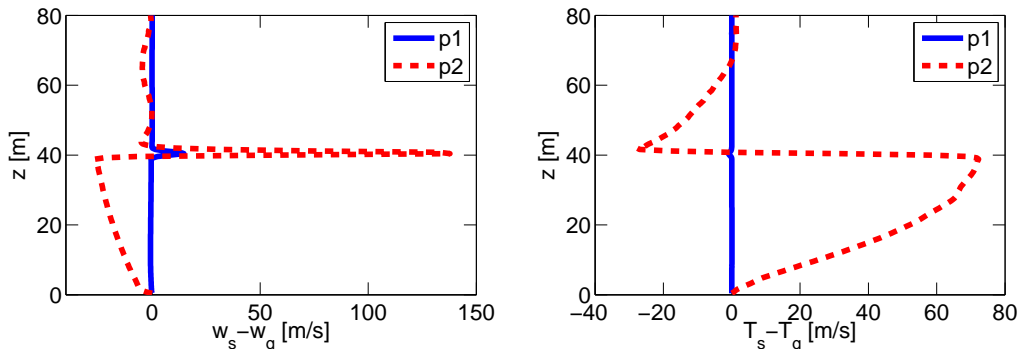

Figure 13: Case C. Time averaged axial profiles computed over the interval $[1.6, 2.0]$ s. Difference between gas vertical velocity and particle vertical velocity (left) and difference between gas temperature and particle temperature (right).

4.3 Three-dimensional simulations

We repeated some of the tests proposed in the previous sections in a three-dimensional configuration, in order to compare with the results obtained in the two-dimensional axisymmetric tests. In this section, we present the results obtained with the vent conditions described in Table 2, Case B. The computational domain is a box of size $400 \times 400 \times 400$ m, we use a non-uniform mesh of $120 \times 120 \times 120$ cells and a time step $\Delta t = 10^{-4}$ s, with maximum grid resolution of 1 m (equal to that employed in 2D) in a subdomain of $50 \times 50 \times 50$m around the vent. Figure 14 shows isosurfaces of the gas vertical velocity at $t = 2$ s. Figure 15 shows the 3D vertical velocity and the logarithm of total particle volumetric fraction averaged along the aximuthal angle. With respect to the 2D simulation in cylindrical symmetry (Figure 11), 3D simulation displays a much diffused jet boundary, associated to the effect of the non-circular inlet. Indeed, with Cartesian mesh discretization, the circular vent has been approximated with squared cells. The flow density (and thus the flow rate injected from cut cells) have been opportunely corrected, but boundary conditions still do not describe the curved inlet rim. This produces some axial switching of the jet cross section in the subsonic region above the Mach disk, analogous to that observed in

29

non-circular subsonic jets, e.g., Gutmark and Grinstein (1999).

However, the shock wave pattern (location and shape of the Mach disk and slip lines) is analogous to the 2D case and the axial profiles of pressure, velocity, mixture density and temperature (Figure 16) are consistent with the results obtained with two dimensional axisymmetric simulations (Figure 12).
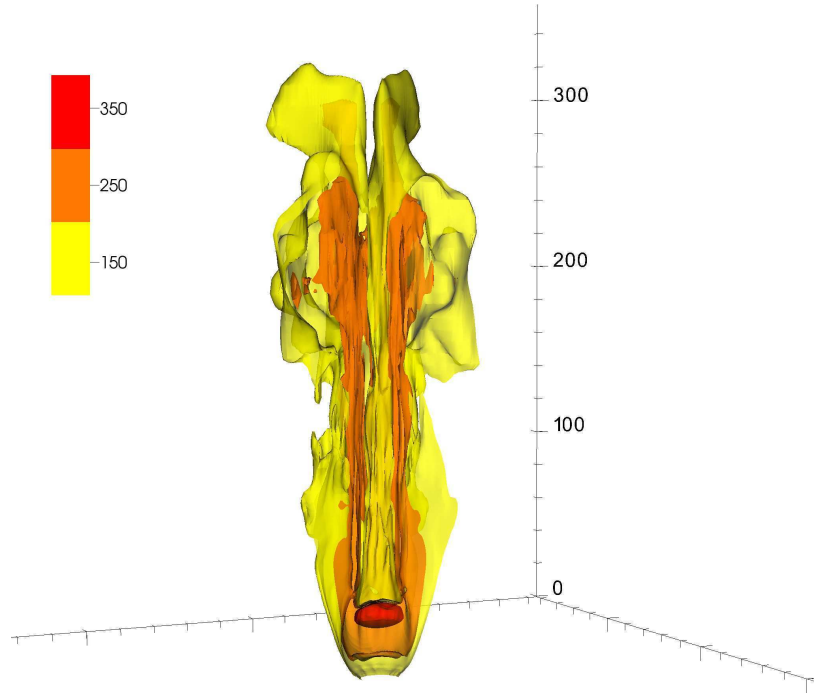

Figure 14: Isosurfaces of gas vertical velocity at $t = 2$ s.

5 Unsteady underexpanded volcanic jets

We have finally investigated the formation of underexpanded jet patterns in the case of unsteady vent conditions, such as those assumed for impulsive Vulcanian eruptions (Clarke et al., 2002; Orescanin et al., 2010). Time-dependent conditions at the volcanic vent have been computed by simulating the expulsion of magmatic gases and pyroclasts from a narrow conduit (analogous to a gas-particle shock-tube) and assuming initial conditions representative of pre-eruptive conditions hypotesized for the 1997 Vulcanian eruption at
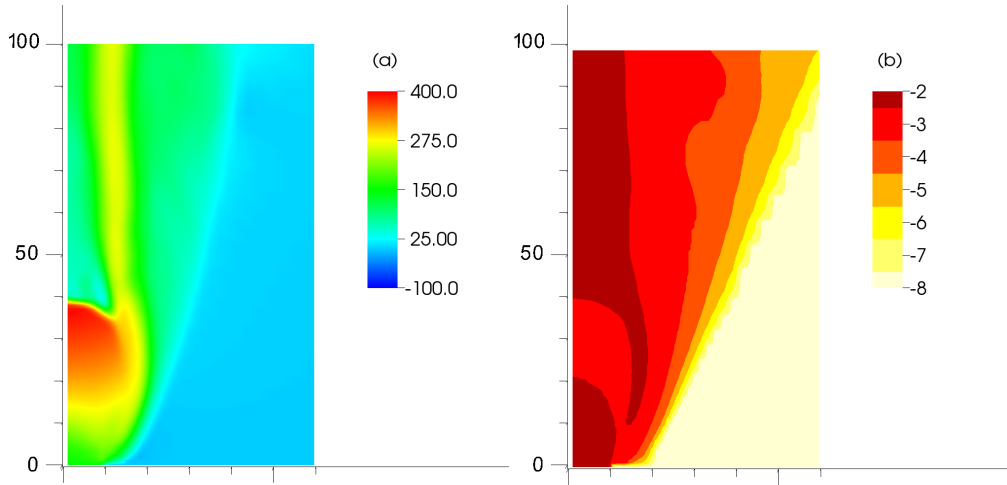
Figure 15: (a) Gas vertical velocity and (b) logarithm of particle volume fraction. Snapshots at $t = 2$ s of a vertical section of averaged quantities along the azimuthal angle.
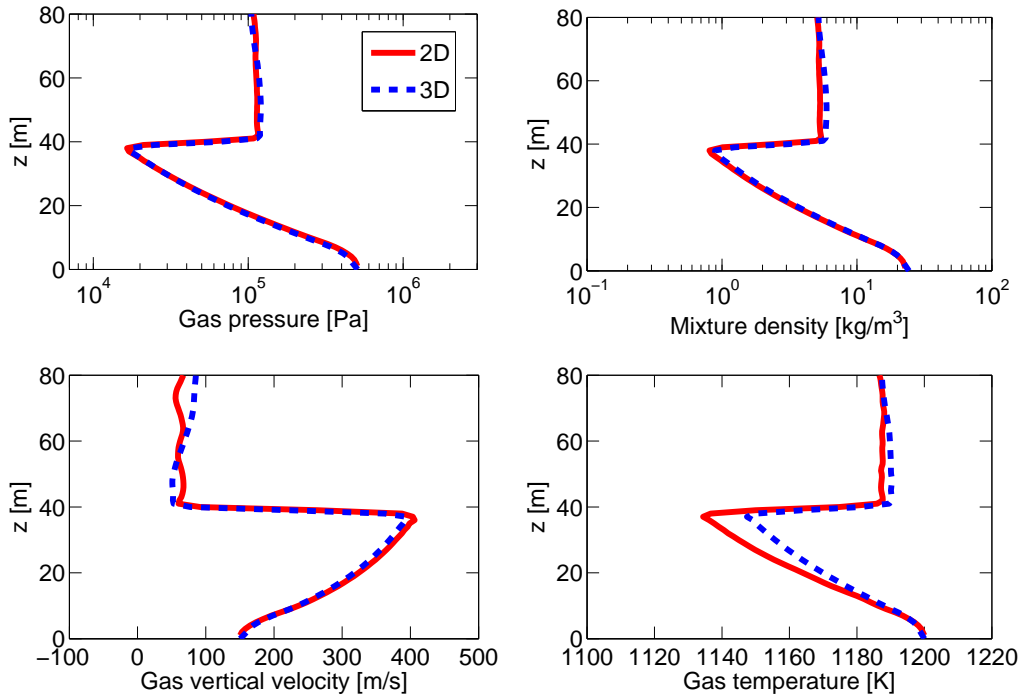

Figure 16: Average axial profiles of gas pressure, gas vertical velocity, mixture density and gas temperature computed over the time interval $[1.6, 2.0]$ s. Comparison between 2D and 3D simulations.

Soufrière Hills Volcano, Montserrat (Clarke et al., 2002). In particular, we have assumed a conduit length of about 1200 m and diameter of 30 m, filled with gas and particles of 30 and 300 μm diameter and density of 2600 kg/m^3. The initial pressure distribution has been computed by assuming 10 MPa overpressure over the hydrostatic profile and gas volume fraction derived from the equilibrium degassing law for liquid magma. Resulting vent conditions as a function of time are reported in Figure 17. The flow is characterized by an initial almost steady state (at choked flow conditions), lasting about 20 seconds. Vent conditions then change abruptly between 20 and 25 s with a steep decrease of the mass flow rate, mainly associated to a significant decrease of gas pressure and mixture density. After 100 s vent conditions are characterized by a slowly varying waning phase.

Figures 18 and 19 show the logarithm of the fine and coarse particle volume fractions, respectively, at $t = 12, 25, 50, 120$ s. After 25 seconds, in correspondance to the rapid change of vent conditions, the volcanic column is destabilized and starts collapsing laterally from above the Mach disk, forming a laterally spreading density current. The column recovers stable convective conditions at about 100 s. Transition between different column regimes during eruptions can therefore be associated to intense column collapse.

In the initial stage, the unsteady simulation gives almost identical results to the steady state (as seen, for example, by comparing gas vertical velocity at 12 s, Figure 20). The axial profile of gas pressure, mixture density, gas vertical velocity and gas temperature confirms that at $t = 12$ s the jet already reached a steady state configuration (with Mach disk at about 150 m). At $t = 120$ s, on the other hand, the unsteady simulation shows a decompression flow pattern characterized by persistence of the Mach disk configuration, located 45 m above the vent. In the corresponding simulation with steady vent conditions (Figure 21), the jet structure is different and, in particular, the Mach disk does not form. The comparison of the axial profiles of gas pressure, mixture density, gas vertical velocity and gas temperature at $t = 120$ s (Figure 23) reveals indeed two different regimes. In the unsteady case, the high-pressure region just above the vent is maintained during column collapse. Rapid expansion and high vertical velocity are associated to the overpressured flow. Such regime is absent in the steady-state simulation, where the decompression follows the typical pattern of low Mach number underexpanded jets, with regular shock reflection and absence of the Mach disk. The observed difference is associated to the complex flow conditions established during collapse. In the event of
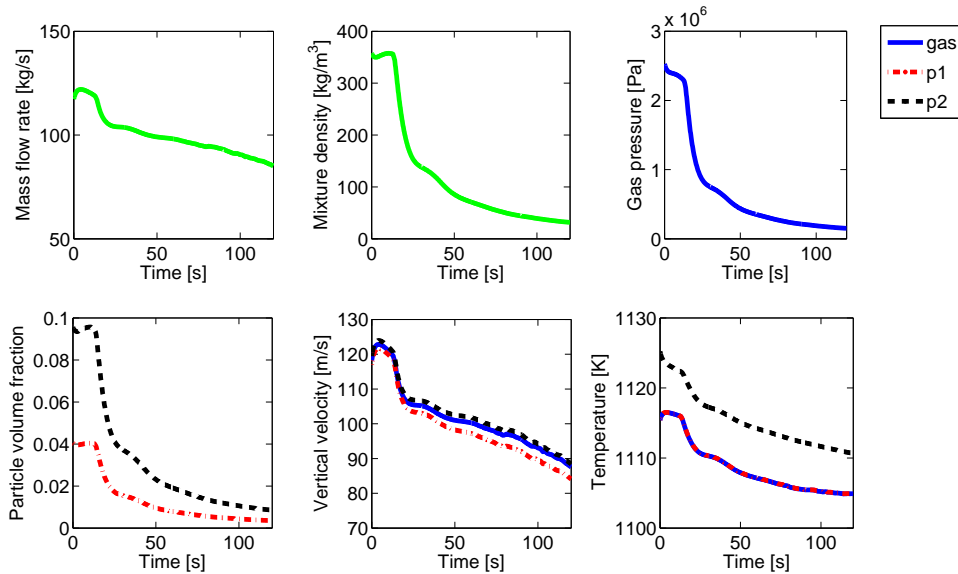
Figure 17: Time evolution of variables at the volcanic vent computed with the volcanic conduit model.

rapid change of vent conditions associated to jet instability, eruption column dynamics do not evolve through a succession of steady states.

6 Conclusion and future developments

The PDAC multiphase flow model has been improved in several aspects of the numerical algorithm to improve the temporal and spatial accuracy of the simulation of explosive volcanic eruptions. In the new model version, a second order Crank-Nicolson type time discretization has been introduced and the fully multidimensional advection schemes proposed by LeVeque (1996) have been employed. The new model has been tested against the complex problem of volcanic jet decompression in both two and three dimensions. Since a proper validation with volcanic jet data is not yet possible, due to the catastrophic nature of the phenomenon and the difficulty of remote measurements, we have verified that the numerical results adequately reproduce some similar phenomenology (i.e., an underexpanded, supersonic gas jet) in the laboratory, where the new numerical scheme demonstrates a better performance (in terms of accuracy and reduced numerical diffusion) at all regimes.

However, several aspects of the dynamics of volcanic jets make
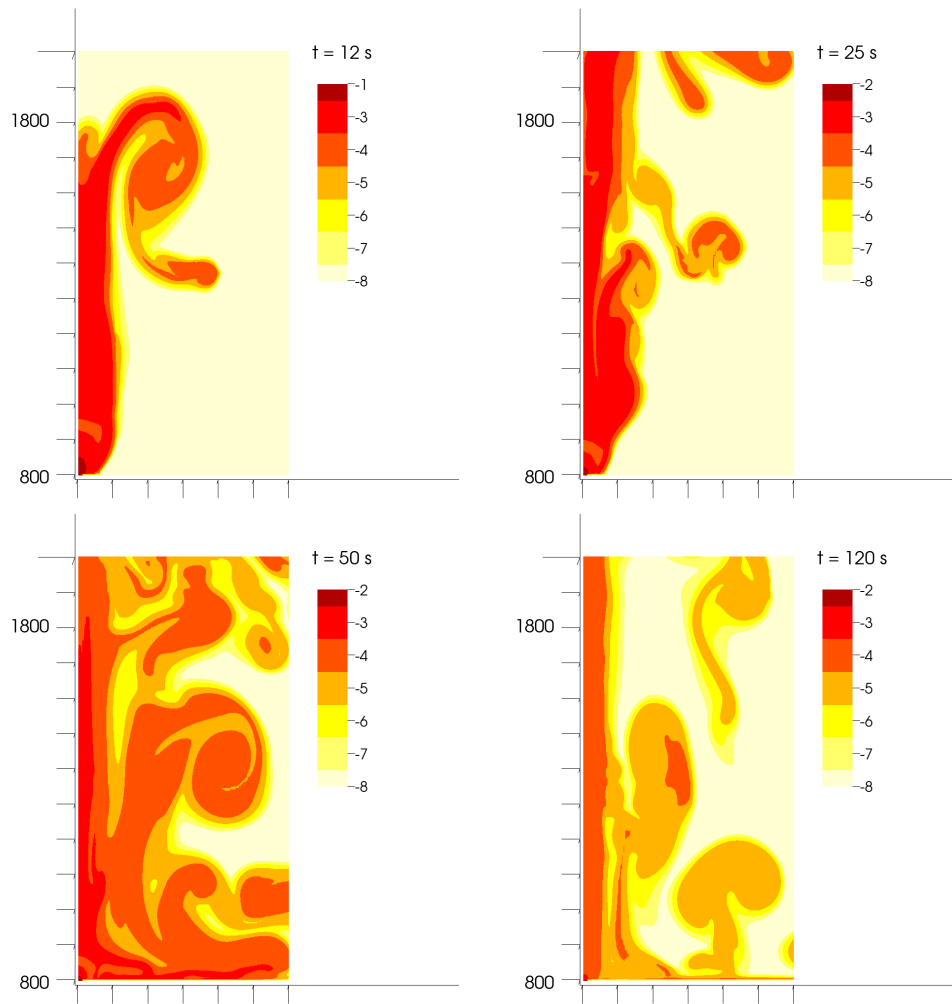
Figure 18: Snapshots of logarithm of fine particles volume fraction at $t = 12$, 25, 50, 120 s.
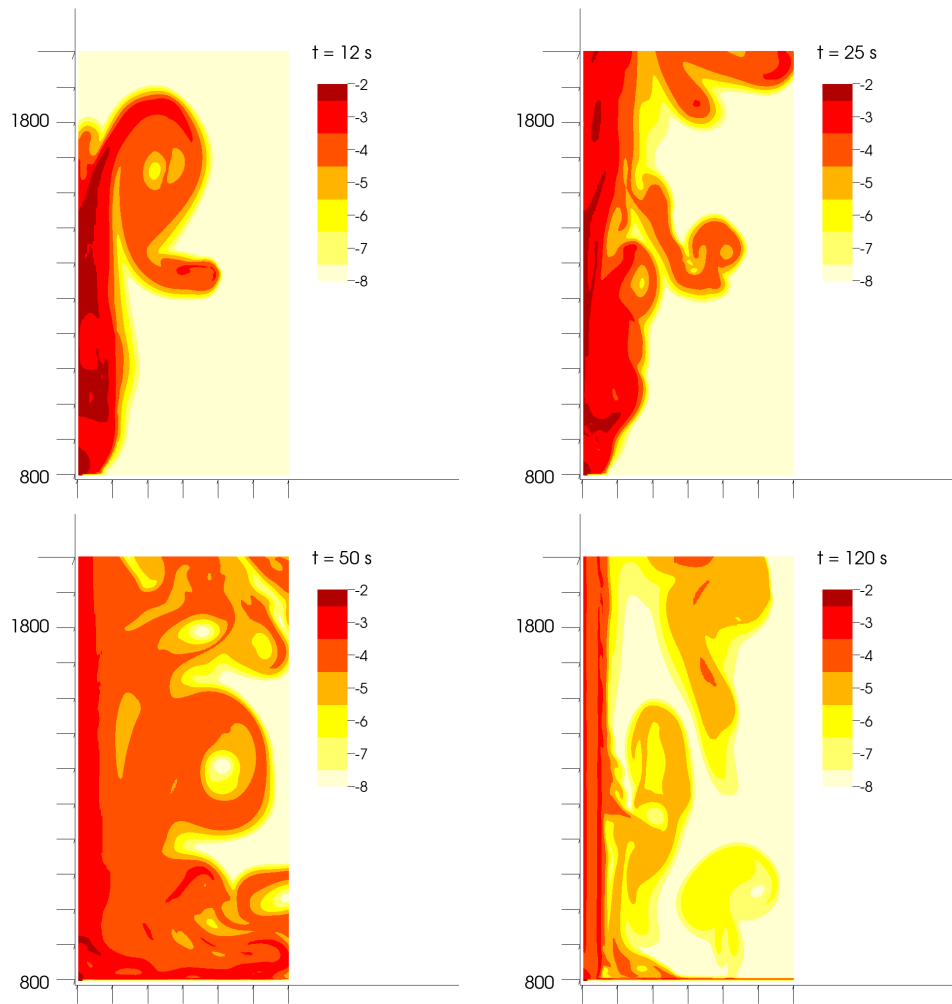
Figure 19: Snapshots of logarithm of coarse particles volume fraction at $t = 12$, 25, 50, 120 s.

Figure 20: Gas vertical velocity. Comparison between (a) simulation with unsteady vent conditions at time $t = 12$ s and (b) simulation with steady vent conditions.
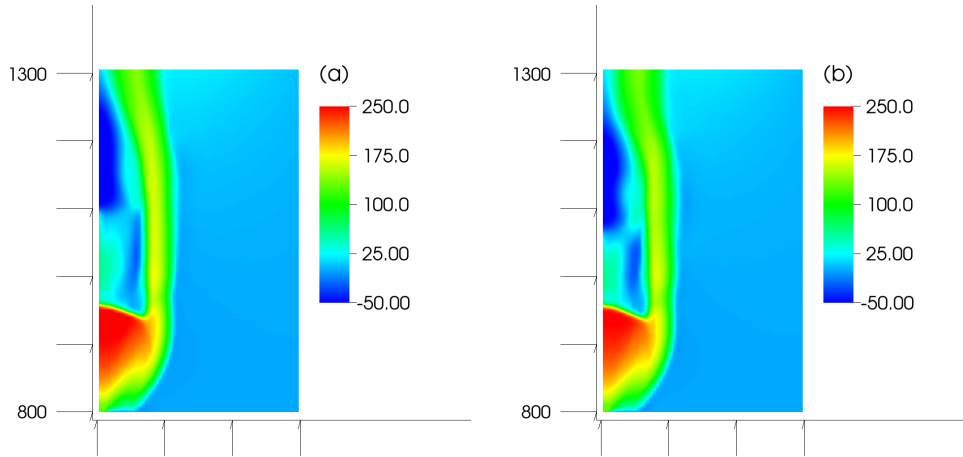

Figure 21: Gas vertical velocity. Comparison between (a) simulation with unsteady vent conditions at time $t = 120$ s and (b) simulation with steady vent conditions.
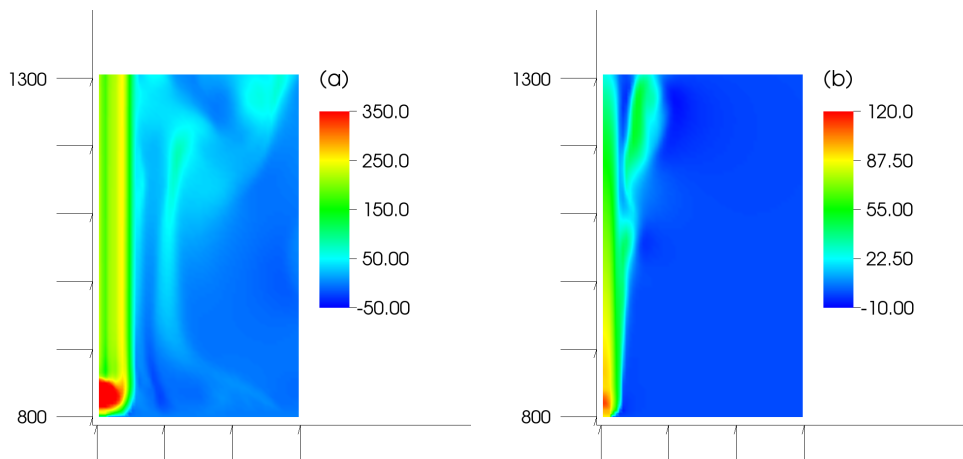
Figure 22: Axial profiles of gas pressure, mixture density, gas vertical velocity and gas temperature. Comparison between simulation with unsteady vent conditions at time $t = 12$ s (NS) and simulation with steady vent conditions (S).
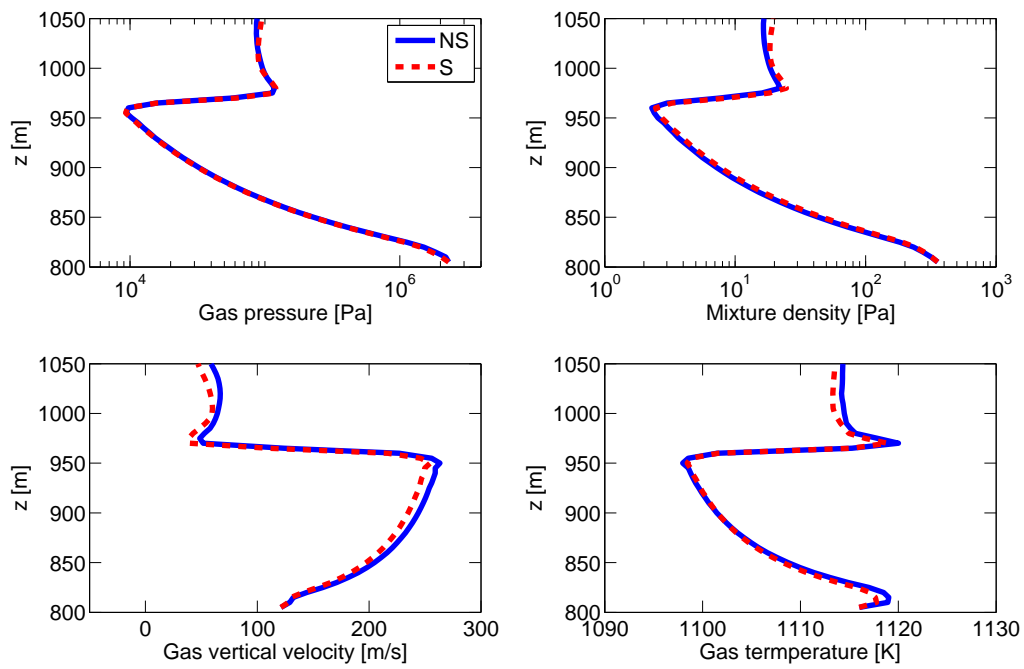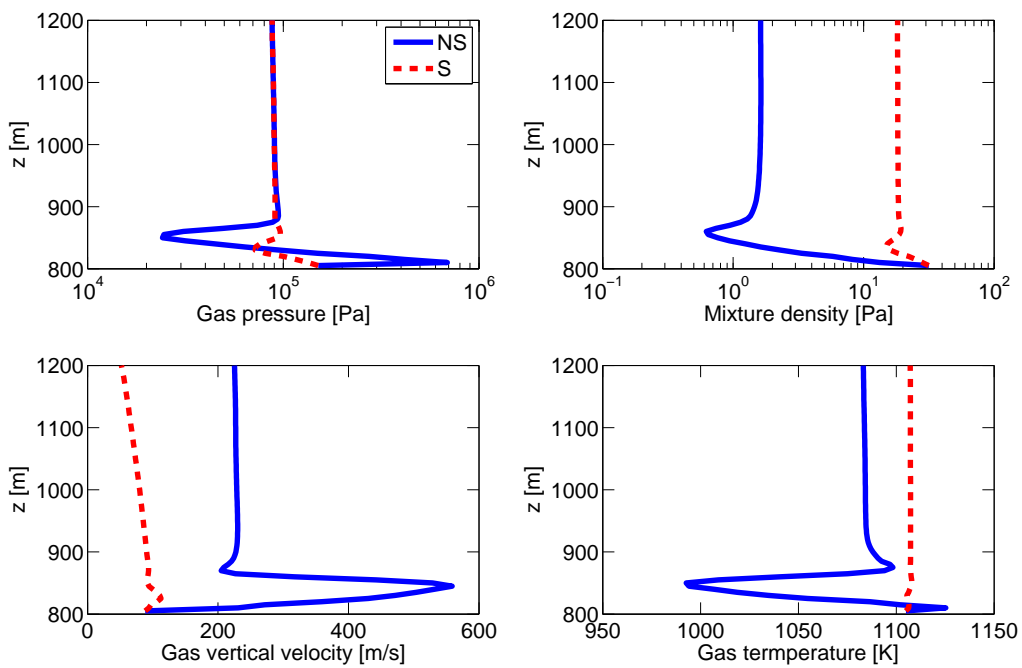
Figure 23: Axial profiles of gas pressure, mixture density, gas vertical velocity and gas temperature. Comparison between simulation with unsteady vent conditions at time $t = 120$ s (NS) and simulation with steady vent conditions (S).

them different from their laboratory analogous: volcanic jets involve the explosive decompression of a multiphase gas-particle mixture at high temperature with eruptive conditions seldom stationary. To account for the presence of solid particles in supersonic volcanic jets, previous workers have described the eruptive mixture as an homogeneous pseudogas, e.g., Kieffer (1984); Ogden et al. (2008b). In the limiting case of fine particles (having a relaxation time much smaller than the characteristic time for decompression), we have demonstrated that the multiphase PDAC model consistently reproduce predictions of the pseudogas model. However, in the case of coarse particles and polydisperse mixtures, multiphase effects become more important and also affect the average jet dynamics. Finally, time-dependent boundary conditions at the volcanic vent have been introduced, in order to be able to simulate eruptive scenarios characterized by transient jet behaviour, such as that hypothesized for Vulcanian eruptions. In such case, we have shown that volcanic jet structure does not evolve through a succession of steady state configurations, and that transition from different flow patterns can result in the catastrophic collapse of the jet with formation of pyroclastic density currents.

The new numerical code appears therefore suited for the multiphase flow simulation of explosive regimes characterized by rapid decompression of the eruptive mixture and possible transition to supersonic regime, including the development of impulsive Vulcanian eruptions and volcanic blasts, which will be addressed in future works. In this context, multiphase effects will be quantified also for polydisperse mixtures, where particle-particle drag might play a key role in the non-equilibrium dynamics of gas-particle flows.

Concerning possible further improvements of the numerical methods employed, we will investigate also the efficiency of purely explicit time discretizations, considering that in most regimes of interest for simulation of volcanic eruptions the Mach number is far from negligible (see Appendix A), as well as more local spatial discretization techniques, such as Discontinuous Galerkin approaches, whose accuracy and parallel efficiency have been widely demonstrated in a great number of applications.

A Dimensional analysis

Let us consider the PDAC equations (1)-(7) for the gas phase g and only one solid phase s. We introduce the non-dimensional quantities

$$\widetilde{x} = \frac{x}{\overline{L}}, \qquad \widetilde{\mathbf{v}}_g = \frac{\mathbf{v}_g}{\overline{U}}, \qquad \widetilde{\rho}_g = \frac{\rho_g}{\overline{\rho}_g}, \qquad \widetilde{T} = \frac{T}{\overline{\Theta}},$$

where $\overline{L}$, $\overline{U}$, $\overline{\rho}_g$ and $\overline{\Theta}$ are characteristic quantities of the system (Table 3). The non-dimensional form of equations (1)-(7) is

$$\begin{cases} \frac{\partial}{\partial t}(\epsilon_g \rho_g) + \nabla \cdot (\epsilon_g \rho_g \mathbf{v}_g) = 0 \\[4pt] \frac{\partial}{\partial t}(\epsilon_s) + \nabla \cdot (\epsilon_s \mathbf{v}_s) = 0 \\[4pt] \frac{\partial}{\partial t}(\epsilon_g \rho_g \mathbf{v}_g) + \nabla \cdot (\epsilon_g \rho_g \mathbf{v}_g \mathbf{v}_g) = -\frac{1}{Ma^2}\epsilon_g \nabla p_g + \frac{1}{Re_g}\nabla \cdot \mathbf{T}_g + \\[4pt] \qquad + \frac{1}{Fr^2}\epsilon_g \rho_g \mathbf{k} + Cd_s(\mathbf{v}_s - \mathbf{v}_g) \\[4pt] \frac{\partial}{\partial t}(\epsilon_s \mathbf{v}_s) + \nabla \cdot (\epsilon_s \mathbf{v}_s \mathbf{v}_s) = -\frac{\overline{\rho}_g}{\rho_s}\frac{1}{Ma^2}\epsilon_s \nabla p_g + \frac{1}{Re_s}\nabla \cdot \mathbf{T}_s + \\[4pt] \qquad + \frac{1}{Fr^2}\epsilon_s \mathbf{k} + Cd_s\frac{\overline{\rho}_g}{\rho_s}(\mathbf{v}_g - \mathbf{v}_s) \\[4pt] \frac{\partial}{\partial t}(\epsilon_g \rho_g T_g) + \nabla \cdot (\epsilon_g \rho_g T_g \mathbf{v}_g) = \frac{Ec}{Ma^2}\epsilon_g\left(\frac{\partial p_g}{\partial t} + \mathbf{v}_g \cdot \nabla p_g\right) + \\[4pt] \qquad + \frac{1}{Pe_g}\nabla \cdot (\epsilon_g \nabla T_g) + \frac{Nu_g}{Pe_g}(T_s - T_g) \\[4pt] \frac{\partial}{\partial t}(\epsilon_s T_s) + \nabla \cdot (\epsilon_s T_s \mathbf{v}_s) = \frac{1}{Pe_s}\nabla \cdot (\epsilon_s \nabla T_s) - \frac{Nu_s}{Pe_s}(T_s - T_g) \end{cases} \tag{30}$$

where the non-dimensional parameters introduced in the analysis are summarized in Table 5. In order to estimate the values of the dimensionless parameters that we have introduced in the non-dimensional model equations, we need to select the characteristic quantities $\overline{L}$, $\overline{U}$, $\overline{\rho}_g$, $\overline{\Theta}$ and the physical coefficients $\overline{\mu}_g$, $\overline{\mu}_s$, c_{pg}, c_{ps}, k_g, k_s, Q_s. The order of magnitude of characteristic quantities depends on the type of problem we are interested in (see Table 3) and we refer to Neri and Macedonio (1996),Todesco et al. (2002),Neri et al. (2003), Esposti Ongaro et al. (2008) for typical values of the physical parameters, that are summarized in Table 4.

We can take as characteristic length either the vent diameter or the volcano's height, depending on the phenomena we are interested in, e.g. volcanic jet or pyroclastic current along the volcano's flank. As characteristic velocity and temperature we choose the mixture velocity and temperature respectively, that can vary of one order of magnitude if we consider the jet and the pyroclastic current. Finally, the mixture density variations are related typically to gas pressure variations, that can vary from 10^5 Pa to 10^7 Pa, and using the equation of state for ideal gas we deduce that it can vary between 10^{-1} kg/m^3 (homogeneous gas) and 10 kg/m^3.

Particle density ρ_s is constant and its order of magnitude can be assumed to be 10^3 kg/m^3. Particle diameter can vary between 10μm and 1 mm and particle volume fractions vary between 0 in case of homogeneous gas and 10^{-2}. Hence, gas volume fraction is often considered equal to 1. Typical values for the mixture viscosity are around 10^{-5} Pa·s, the constant pressure specific heat is assumed to be equal to 10^3 J/kg·K and the conductivity is considered equal to 10^{-2} W/m·K. The gas-particle drag coefficient $D_{g,s}$ and the heat transfer coefficient Q_s can be estimated from empirical relations reported in Appendix B and they vary between $1 - 10^4$ kg/m^3·s and $10^2 - 10^3$ W/m^3·K, respectively. Finally, the speed of sound of the mixture can be computed, as proposed by Pelanti and LeVeque (2006), as

$$c_{s,mix} = \sqrt{\tilde{R}T\frac{\rho_g}{\epsilon_g(\epsilon_g\rho_g + \epsilon_s\rho_s)}}. \tag{31}$$

We can observe in particular that the maximum speed of sound is obtained in the case of homogeneous gas and it can increase almost up to 10^3 m/s for high temperatures, whereas it diminishes as particle volume fraction increases down to a few tens of meters per second.

The range of admissible values for the non-dimensional parameters that appears in the Equations 30 are shown in Table 5. We can observe that the Reynolds number, the Prandtl number and the Péclet number are much larger than 1, thus meaning that the second order diffusive terms are negligible with respect to the other terms in the regimes we are interested in. Moreover, the results show how the process is mainly governed by the interphase exchange phenomena, i.e. the drag interaction and the heat transfer. Finally, we can not neglet "a priori" the gravity terms and the compression and expansion term, even if in some region of the domain they could become less important. The Mach number varies from 10^{-1} when we consider pyroclastic density current parameters, that is low velocities and large particle volume fraction, up to 10 when we focus on the volcanic jet, where we reach the maximum mixture velocity and the maximum speed of sound.

B   Drag and heat transfer coefficients

B.1   Drag coefficients

The drag coefficient between gas and solid particles is a complex function of the particle concentration and the gas-particle Reynolds

Quantity		e.g.	Units	Range
Length	$\overline{L}$	vent diameter, volcano's height	[m]	$10\text{-}10^3$
Velocity	$\overline{U}$	mixture velocity	[m/s]	$10\text{-}10^2$
Temperature	$\overline{\Theta}$	mixture temperature	[K]	$10^2\text{-}10^3$
Gas density	$\overline{\rho}_g$	gas density at the vent	[kg/m^3]	$10^{-1}\text{-}10^1$

Table 3: Definition and range of admissible values of characteristic quantities.

Quantity	Units	Range
ρ_s	[kg/m^3]	10^3
d_s	[m]	$10^{-5}\text{-}10^{-3}$
ϵ_s		$0\text{-}10^{-1}$
ϵ_g		~ 1
μ	[Pa·s]	10^{-5}
c_p	[J/kg·K]	10^3
k	[W/m·K]	10^{-2}
$D_{g,s}$	[kg/m^3·s]	$1\text{-}10^4$
Q_s	[W/m^3· K]	$10^2\text{-}10^3$
$c_{s,mix}$	[m/s]	$10\text{-}10^3$

Table 4: Order of magnitude of physical parameters that are used in the dimensional analysis.

Parameter	Symbol	Definition	Range
Reynolds number	Re	$\overline{\rho}\,\overline{U}\,\overline{L}/\overline{\mu}$	$10^6\text{-}10^{11}$
Mach number	Ma	$\overline{U}/\overline{c}$	$10^{-1}\text{-}10$
Froude number	Fr	$\overline{U}/\sqrt{g\,\overline{L}}$	$10^{-1}\text{-}10$
Drag coefficient	Cd_s	$D_{g,s}\overline{L}/\overline{\rho}_g\overline{U}$	$10^{-1}\text{-}10^7$
Peclet number	Pe	$\overline{U}\,\overline{L}\,\overline{\rho}\,c_p/k$	$10^6\text{-}10^{11}$
Eckert number	Ec	$\overline{U}^2/c_p\overline{\Theta}$	$10^{-4}\text{-}10^{-2}$
Nusselt number	Nu	$Q\,\overline{L}^2/k$	$10^6\text{-}10^{11}$

Table 5: Definition and range of admissible values of non-dimensional parameters.

number, defined as

$$Re_s = \frac{\epsilon_g \rho_g d_s |\mathbf{v}_g - \mathbf{v}_s|}{\mu_g}. \tag{32}$$

where d_s is the particle diameter and μ_g is the dynamic viscosity of the gas phase. In the dilute regime $\epsilon_g \geq 0.8$, we adopt the drag expression given in Wen and Yu (1966):

$$D_{g,s} = D_{s,g} = \frac{3}{4} C_{d,s} \frac{\epsilon_g \epsilon_s \rho_g |\mathbf{v}_g - \mathbf{v}_s|}{d_s} \epsilon_g^{-2.7}, \quad s = 1 \dots N, \tag{33}$$

with

$$C_{d,s} = \frac{24}{Re_s} \left[1 + 0.15 Re_s^{0.687} \right], \quad \text{if } Re_s < 1000,$$

$$C_{d,s} = 0.44, \qquad\qquad\qquad \text{if } Re_s \geq 1000, \tag{34}$$

In the dense regime $\epsilon_g < 0.8$, we adopt the drag expression proposed in Ergun (1952):

$$D_{g,s} = 150 \frac{\epsilon_s^2 \mu_g}{\epsilon_g d_s^2} + 1.75 \frac{\epsilon_s \rho_g |\mathbf{v}_g - \mathbf{v}_s|}{d_s}, \quad s = 1, \dots N, \tag{35}$$

Furthermore, the semi-empirical correlation of Syamlal (1985) is used to model the particle-particle drag:

$$D_{s,p} = F_{sp} \alpha (1 + C_R) \rho_s \epsilon_s \rho_p \epsilon_p \frac{(d_s + d_p)^s}{\rho_s d_s^3 + \rho_p d_p^3} |\mathbf{v}_s - \mathbf{v}_p|, \quad s = 1 \dots N, \ p \neq s, \tag{36}$$

where α is an empirical coefficient accounting for non-head-on collisions, C_R is the restitution coefficient for a collision and $F_{s,p}$ is a function of the volume fraction of the two phases and of the maximum volume fraction of a random closely packed mixture $\epsilon_{s,p}$, defined in Syamlal (1985) as:

$$F_{s,p} = \frac{3\epsilon_{s,p}^{1/3} + (\epsilon_s + \epsilon_p)^{1/3}}{2\left(\epsilon_{s,p}^{1/3} - (\epsilon_s + \epsilon_p)^{1/3}\right)}. \tag{37}$$

In order to define $\epsilon_{s,p}$, we introduce the following quantities:

$$a = \left(\frac{d_s}{d_p} \right)^{1/2}, \quad \text{with } d_s \geq d_p,$$

$$X_s = \frac{\epsilon_s}{\epsilon_s + \epsilon_p}, \tag{38}$$

and $\Phi_s = 0.63$, representing the solid volume fraction at maximum packing in a single particle system for the s-th phase. Then we define

$$
\epsilon_{s,p} = \begin{cases}
[(\Phi_s - \Phi_p) + (1-a)(1-\Phi_s)\Phi_p]\frac{[\Phi_s + (1-\Phi_p)\Phi_s]}{\Phi_s}X_s + \Phi_p, \\
\qquad \text{if } X_s \leq \frac{\Phi_s}{\Phi_s + (1-\Phi_s)\Phi_p}, \\
(1-a)[\Phi_s + (1-\Phi_s)\Phi_p](1-X_s) + \Phi_s, \\
\qquad \text{if } X_s \geq \frac{\Phi_s}{\Phi_s + (1-\Phi_s)\Phi_p}.
\end{cases} \tag{39}
$$

B.2   Heat transfer coefficients

The heat transfer between the gas and the solid phases is given by the product of a transfer coefficient Q_s and a driving force, which is the difference in temperature between the two phases. The coefficient Q_s represents the volumetric interphase heat transfer coefficient, which equals the product of the specific exchange area and the fluid-particle heat transfer coefficient. We define $Q_s = 6Nu_s k_g \epsilon_s / d_s$, where the empirical expression for the Nusselt number Nu_s is taken from Gunn (1978):

$$
Nu_s = \left(2 + 5\epsilon_s^2\right)\left(1 + 0.7Re_s^{0.2}Pr^{1/3}\right) + \left(0.13 + 1.2\epsilon_s^2 Re_s^{0.7}Pr^{1/3}\right), \tag{40}
$$

for $Re_s \leq 10^5$, where

$$
Re_s = \frac{\rho_g d_s |\mathbf{v}_g - \mathbf{v}_s|}{\mu_s}, \qquad Pr = \frac{c_{p,g}\mu_g}{k_g}, \tag{41}
$$

and k_g is the thermal conductivity of the gas phase.

Acknowledgements

References

A. Arakawa and V.R. Lamb. A potential enstrophy and energy conserving scheme for the shallow water equations. *Monthly Weather Review*, 109:18–36, 1981.

A.B. Clarke, A. Neri, B. Voight, G. Macedonio, and T. Druitt. Computational modelling of the transient dynamics of the August 1997 Vulcanian explosions at Soufrière Hills Volcano, Montserrat: influence of initial conduit conditions on near-vent pyroclastic dispersal. *Geological Society Memoires*, 21:319–348, 2002.

P. Colella. Multidimensional upwind methods for hyperbolic conservation laws. *Journal of Computational Physics*, 87:171–200, 1990.

J. Crank and P. Nicolson. A practical method for numerical evaluation of solutions of partial differential equations of the heat-conduction type. *Proceedings of the Cambridge Philosophical Society*, 43(1):50–67, 1947.

S. Dartevelle, W.I. Rose, J. Stix, K. Kelfoun, and J.W. Vallance. Numerical modeling of geophysical granular flows: 2. Computer simulations of Plinian clouds and pyroclastic flows and surges. *Geochemistry, Geophysics, Geosystems*, 5, Q08004, 2004. doi: 10:1029/2003GC000637.

F. Dobran, A. Neri, and G. Macedonio. Numerical simulation of collapsing volcanic columns. *Journal of Geophysical Research*, 98 (B3):4231–4259, 1993.

D.M. Doronzo, J. Martí, R. Sulpizio, and P. Dellino. Aerodynamics of stratovolcanoes during multiphase processes. *Journal of Geophysical Research*, 117, B01207, 2012. doi: 10.1029/2011JB008769.

J. Dufek and G.W. Bergantz. Dynamics and deposits generated by the Kos Plateau Tuff eruption: Controls of basal particle loss on pyroclastic flow transport. *Geochemistry, Geophysics, Geosystems*, 8, Q12007, 2007. doi: 10.1029/2007GC001741.

A. Einstein. Eine neue Bestimmung der Molekldimensionen. *Annals of Physics*, 19:289–306, 1906.

S. Ergun. Fluid flow through packed columns. *Chemical Engineering and Processing*, 48:89–94, 1952.

T. Esposti Ongaro, C. Cavazzoni, G. Erbacci, A. Neri, and M.V. Salvetti. A parallel multiphase flow code for the 3D simulation of explosive volcanic eruptions. *Parallel Computing*, 33:541–560, 2007.

T. Esposti Ongaro, A. Neri, G. Menconi, M. De' Michieli Vitturi, P. Marianelli, C. Cavazzoni, G. Erbacci, and P.J. Baxter. Transient 3D numerical simulations of column collapse and pyroclastic density current scenarios at Vesuvius. *Journal of Volcanology and Geothermal Research*, 178(3):378–396, 2008.

T. Esposti Ongaro, A.B. Clarke, B. Voight, A. Neri, and C. Widiwijayanti. Multiphase flow dynamics of pyroclastic density currents during the May 18, 1980 lateral blast of Mount St. Helens. *Journal of Geophysical Research*, 117(6), B06208, 2012. doi: 10.1029/2011JB009081.

H.M. Gonnermann and M. Manga. The fluid mechanics inside a volcano. *Annual Review of Fluid Mechanics*, 39:321–356, 2007.

H.-F. Graf, M. Herzog, J.M. Oberhuber, and C. Textor. Effect of environmental conditions on volcanic plume rise. *Journal of Geophysical Research*, 104(D20):24309–24320, 1999.

D.J. Gunn. Transfer of heat or mass to particles in fixed and fluidised beds. *International Journal of Heat and Mass Transfer*, 21(4): 467–476, 1978.

E.J. Gutmark and F.F. Grinstein. Flow control with noncircular jets. *Annual Review of Fluid Mechanics*, 31:239–272, 1999.

F.H. Harlow and A.A. Amsden. Numerical calculation of multiphase fluid flow. *Journal of Computational Physics*, 17:19–52, 1975.

F.H. Harlow and J.E. Welch. Numerical calculation of time-dependent viscous incompressible flow of fluid with free surface. *Physics of Fluids*, 8(12):2182–2189, 1965.

S.W. Kieffer. Factors governing the structure of volcanic jets. *Explosive volcanism: inception, evolution, and hazards*, pages 143–157, 1984.

R.J. LeVeque. High-resolution conservative algorithms for advection in incompressible flow. *SIAM Journal on Numerical Analysis*, 33 (2):627–665, 1996.

C.H. Lewis and D.J. Carlson. Normal shock location in underexpanded gas and gas particle jets. *AIAA Journal*, 2:776–777, 1964.

F.E. Marble. Dynamics of dusty gases. *Annual Review of Fluid Mechanics*, 2:397–446, 1970.

A. Neri and G. Macedonio. Physical modeling of collapsing volcanic columns and pyroclastic flows. In *Monitoring and mitigation of volcano hazards*, pages 389–427, Berlin-Heidelberg, Germany, 1996. Springer-Verlag.

A. Neri, T. Esposti Ongaro, G. Macedonio, and D. Gidaspow. Multiparticle simulation of collapsing volcanic columns and pyroclastic flow. *Journal of Geophysical Research*, 108, B4, 2202, 2003.

J.M. Oberhuber, M. Herzog, H.F. Graf, and K. Schwanke. Volcanic plume simulation on large scales. *Journal of Volcanology and Geothermal Research*, 87:29–53, 1998.

D.E. Ogden, G.A. Glatzmaier, and K.H. Wohletz. Effects of vent overpressure on buoyant eruption columns: implications for plume stability. *Earth and Planet Science Letters*, 268:283–292, 2008a.

D.E. Ogden, K.H. Wohletz, G.A. Glatzmaier, and E.E. Brodsky. Numerical simulations of volcanic jets: importance of vent overpressure. *Journal of Geophysical Research*, 113(2), B02204, 2008b. doi: 10.1029/2007JB005133.

M.M. Orescanin, J.M. Austin, and S.W. Kieffer. Unsteady high-pressure flow experiments with applications to explosive volcanic eruptions. *Journal of Geophysical Research*, 115(6), B06206, 2010. doi: 10.1029/2009JB006985.

N. Oreskes, K. Shrader-Frechette, and K. Belitz. Verification, validation, and confirmation of numerical models in the Earth Sciences. *Science*, 263:641–646, 1994.

E.A. Parfitt and L. Wilson. *Fundamentals of Physical Volcanology.* John Wiley, 2008.

M. Pelanti and R.J. LeVeque. High-resolution finite volume methods for dusty gas jets and plumes. *SIAM Journal on Scientific Computing*, 28(4):1335–1360, 2006.

A. Quarteroni, R. Sacco, and F. Saleri. *Numerical Mathematics.* Springer-Verlag, 2002.

P.L. Roe. Characteristic-based schemes for the Euler equations. *Annual Review of Fluid Mechanics*, 18:337–365, 1986.

J. Saltzman. An unsplit 3D upwind method for hyperbolic conservation laws. *Journal of Computational Physics*, 115:153–168, 1993.

R.S.J. Sparks, M.I. Bursik, S.N. Carey, J.S. Gilbert, L.S. Glaze, H. Sigurdsson, and A.W. Woods. *Volcanic Plumes*. John Wiley, 1997.

Y.J. Suzuki and T. Koyaguchi. Numerical determination of the efficiency of entrainment in volcanic eruption columns. *Geophysical Research Letters*, 37(5), L05302, 2010. doi: 10.1029/2009GL042159.

Y.J. Suzuki, T. Koyaguchi, M. Ogawa, and I. Hachisu. A numerical study of turbulent mixing in eruption clouds using a three-dimensional fluid dynamics model. *Journal of Geophysical Research*, 110(8), B08201, 2005. doi: 10.1029/2004JB003460.

P. Sweby. High resolution schemes using flux-limiters for hyperbolic conservation laws. *SIAM Journal on Numerical Analysis*, 21(5): 995–1011, 1984.

M. Syamlal. Multiphase hydrodynamics of gas-solid flow. Ph.D. Thesis, Illinois Institute of Technology, Chicago, Illinois, USA, 1985.

M. Syamlal. MFIX documentation: numerical technique. Technical report, U.S. Department of energy, Office of fossil energy, Federal Energy Technology Center, Morgantown, West Virginia, USA, January 1998.

M. Syamlal, W. Rogers, and T.J. O'Brien. MFIX documentation: technical note. Technical report, U.S. Department of energy, Office of fossil energy, Morgantown Energy Technology Center, Morgantown, West Virginia, USA, December 1993.

M. Todesco, A. Neri, T. Esposti Ongaro, P. Papale, G. Macedonio, R. Santacroce, and A. Longo. Pyroclastic flow hazard assessment at Vesuvius (Italy) by using numerical modeling. I. Large-scale dynamics. *Bulletin of Volcanology*, 64:155–177, 2002.

G.A. Valentine. *Eruption column physics*, volume 4, pages 91–138. A. Freudt and M. Rosi, Elsevier, Netherlands, 1998.

G.A. Valentine and K.H. Wohletz. Numerical models of Plinian eruption columns and pyroclastic flows. *Journal of Geophysical Research*, 94(B2):1867–1887, 1989.

C.Y. Wen and Y.H. Yu. Mechanics of fluidization. *Chemical Engineering Progress Symposium Series*, 62:100–111, 1966.

L. Wilson. Explosive volcanic eruptions – III – Plinian eruption columns. *Geophysical Journal of the Royal Astronomical Society*, 45:543–556, 1976.

A.W. Woods. The dynamics and thermodynamics of eruption columns. *Bulletin of Volcanology*, 50(3):169–193, 1988.

A.W. Woods and S.M. Bower. The decompression of volcanic jets in a crater during explosive volcanic eruptions. *Earth and Planet Science Letters*, 131:189–205, 1995.

MOX Technical Reports, last issues

**Dipartimento di Matematica "F. Brioschi",
Politecnico di Milano, Via Bonardi 9 - 20133 Milano (Italy)**

49/2012   MIGLIORATI, G.;NOBILE, F.;VON SCHWERIN, E.;TEMPONE, R.
Approximation of Quantities of Interest in stochastic PDEs by the random discrete L2 projection on polynomial spaces

50/2012   CARCANO, S.; BONAVENTURA, L.; NERI, A.; ESPOSTI ONGARO, T.
A second order accurate numerical model for multiphase underexpanded volcanic jets

48/2012   GHIGLIETTI, A.; PAGANONI, A.M.
Statistical properties of two-color randomly reinforced urn design targeting fixed allocations

47/2012   ASTORINO, M.; CHOULY, F.; QUARTERONI, A.
Multiscale coupling of finite element and lattice Boltzmann methods for time dependent problems

46/2012   DASSI, F.; PEROTTO, S.; FORMAGGIA, L.; RUFFO, P.
Efficient geometric reconstruction of complex geological structures

45/2012   NEGRI, F.; ROZZA, G.; MANZONI, A.; QUARTERONI, A.
Reduced basis method for parametrized elliptic optimal control problems

43/2012   SECCHI, P.; VANTINI, S.; VITELLI, V.
A Case Study on Spatially Dependent Functional Data: the Analysis of Mobile Network Data for the Metropolitan Area of Milan

44/2012   FUMAGALLI, A.; SCOTTI, A.
A numerical method for two-phase flow in fractured porous media with non-matching grids

42/2012   LASSILA, T.; MANZONI, A.; QUARTERONI, A.; ROZZA, G.
Generalized reduced basis methods and n width estimates for the approximation of the solution manifold of parametric PDEs

41/2012   CHEN, P.; QUARTERONI, A.; ROZZA, G.
Comparison between reduced basis and stochastic collocation methods for elliptic problems